Recent changes in glacier facies zonation on Devon Ice Cap, Nunavut, detected from SAR imagery and field validation methods

Johannes Tyler de Jong

Thesis submitted to the

Faculty of Graduate and Postdoctoral Studies

in partial fulfillment of the requirements

for the M.Sc. Degree in Physical Geography

Department of Geography

Faculty of Arts

University of Ottawa

Supervisor:

Dr. Luke Copland (University of Ottawa)

Thesis Committee:

Dr. David Burgess (Natural Resources Canada)

Dr. Denis Lacelle (University of Ottawa)

Abstract

Glacier facies represent distinct regions of a glacier surface characterized by near surface structure and density that develop as a function of spatial variations in surface melt and accumulation. In post freeze-up (autumn) synthetic aperture radar (SAR) satellite imagery, the glacier ice zone and dry snow zone have a relatively low backscatter due to the greater penetration of the radar signal into the surface. Conversely, the saturation and percolation zones are identifiable based on their high backscatter due to the presence of ice lenses and pipes acting as efficient scatterers. In this study, EnviSat ASAR imagery is used to monitor the progression of facies zones across Devon Ice Cap (DIC) from 2004 to 2011. This data is validated against in situ surface temperatures, mass balance data, and ground penetrating radar surveys from the northwest sector of DIC. Based on calibrated (sigma nought) EnviSat ASAR backscatter values, imagery from autumn 2004 to 2011 shows the disappearance of the 'pseudo' dry snow zone at high elevations, the migration of the glacier and superimposed ice zones to higher elevations, and reduction in area of the saturation/percolation zone. In 2011, the glacier and superimposed ice zone were at their largest extent, occupying 92% of the ice cap, leaving the saturation/percolation zone at 8% of the total area. This is indicative of anomalously high summer melt and strongly negative mass balance conditions on DIC, which results in the infilling of pore space in the exposed firn and consequent densification of the ice cap at higher elevations.

Acknowledgements

This master's thesis is dedicated to my late grandfather, Thomas Edward Cavanagh, whose passion for adventure and travelling was passed down to me. He would have truly enjoyed my stories from the Arctic and would have had a deep appreciation for this research.

I would like to sincerely thank my supervisor, Dr. Luke Copland, who inspired me to pursue a master's in glaciology. This time in my life has been truly inspirational as it has brought me to places such as the Canadian Arctic, Antarctica, Svalbard, Alaska and the Yukon. I owe so much to Luke, it's hard to put into words how much he has done for me and how grateful I am towards him.

I would also like to thank Dr. David Burgess for giving me the opportunity to do field work in the Canadian High Arctic. It was a great privilege to learn about what it takes to do field work in the, sometimes harsh conditioned, arctic. My time spent with Dave in the field will be some of my most memorable and cherished moments in my life, I'm sure. Thanks for showing me the ropes!

To my mom and dad, thank you for your love and support. I owe you two so much, and will be forever grateful for the foundation you have giving me which has led to all my accomplishments in life. To my brother, Garrett, you're my best friend and thanks for helping me through the tough times. By simply being around and hanging out with you it seemed as though all my stress and worries would just go away. To my sister, Alexia, you are so caring and loving, I want you to know it means a lot to me. Your inspiration gave me strength and determination to get through any challenge I faced during my academic career.

There are many people during my seven years at the University of Ottawa who I would like to especially thank. These people in some way or another helped me through this journey, and they include: Jean Bjornson, Sylvie Theriault, Chantale Arcand, Denis Lacelle, Wesley Van Wychen, Adrienne White, Laura Thomson, Nicole Schaffer, Alex Waechter, Emilie Herdes, Samantha Darling, Alex Bevington, Leo Sold, Mauro Fisher, Max Wert, Pat Ferguson, Jake Walton, EJ Bercier, Max Duguay and Piqsiq.

Table of Contents

List of Tables

List of Figures

1.0 Introduction

The Canadian Arctic Archipelago (CAA) (Figure 1.1) has a total area of ~146,000 km^2 covered by glaciers and ice caps, making it one of the largest glaciated regions outside of Greenland and Antarctica (Lenaerts et al, 2013). From 1960 to 2003 there was a weak but significant trend towards an increasingly negative mass balance in the CAA (Koerner 2005). Subsequently, 30-48% of total mass loss since 1963 has occurred from 2005 to 2011 for the four glaciers regularly monitored in this region (northwest Devon Ice Cap, Meighen Ice Cap, Melville south Ice Cap, and White Glacier, Axel Heiberg Island) (Sharp et al, 2011). Jacob et al, (2012) found that from 2003 to 2010, the CAA contributed 45% of global mass loss from all glaciers and ice caps outside of the Greenland and Antarctic ice sheets. Most of this mass loss (~92%) has been attributed to runoff, as iceberg discharge is normally assumed to be constant due to a lack of knowledge surrounding its temporal variability in the CAA (Van Wychen et al, 2012; Gardner et al, 2012; Lenaerts et al, 2013). This increase in runoff can be credited to an increase in summer air temperatures and associated shrinkage of the accumulation area of glaciers and ice caps (Sharp et al, 2011; Lenaerts et al, 2013).

In a warming climate, it is unclear how glacier motion will change in the CAA (Van Wychen et al, 2012). On the Greenland Ice Sheet, increases in surface melt have been linked to glacier speed-up events, as the supraglacial meltwater can make its way to the glacier bed and lubricate the basal interface, thus enhancing basal sliding and glacier motion (Zwally et al, 2002; Rignot and Kanagaratnam 2006; van de Wal et al 2008). An increase in glacier motion is significant since an increase in ice discharge (= ice velocity x ice thickness x glacier width) can increase the rate of terrestrial ice reaching the sea, resulting in increased calving from tidewater glaciers and contributing to sea-level rise. Acceleration in outflow from higher to lower elevations can also

reduce the area-altitude distribution, thus causing more ice to be at low elevations where air temperatures are warmer and melt rates are higher. There is some debate as to whether large glaciers will continue accelerating under negative mass balance conditions, however, as some authors have suggested that increased surface melt will result in larger, more efficient subglacial drainage channels and an associated reduction in subglacial water pressure and glacier velocity (Schoof, 2010) . For example, Sundal et al (2011) found that in high melt years a drop in summer velocities occurred on a land-terminating sector of the Greenland ice sheet. The effect of melt-induced glacier acceleration thus remains uncertain, although some suggest that speed-up events depend on short-term spikes in meltwater inputs to the bed, resulting in high basal water pressures (Schoof 2010).

In the arctic, summer 2012 experienced two major occurrences never before seen in modern times:

(1) The lowest arctic sea ice extent in the satellite era (NSIDC 2012)

(2) The lack of a dry snow zone (area that experiences no annual melt) on the Greenland Ice Sheet (Nghiem et al, 2012)

The 2012 record low sea-ice extent was 3.41 x 10^6 km^2, 18 % below the previous record low in 2007. This decline was partially attributed to an intense summer cyclone in August 2012, and bottom melt due to strong upward ocean heat transport (Zhang et al, 2013). The gradual thinning and reductions of sea ice extent since 1979, followed by an enhanced reduction in sea-ice extent from 2006 onwards, was also seen as a precursor to the 2012 record sea ice minimum (Cavalieri and Parkinson, 2012; Zhang et al, 2013).

The extreme melt across the Greenland Ice Sheet in summer 2012 was the first time melt was recorded at the summit since 1889 (Clausen et al, 1988). Moreover, melt layers in the Greenland GISP2 ice core were only seen eight times between the years 500 and 1994 (Meese et al, 1994). With an increased melt rate on the Greenland Ice Sheet, densification in the lower accumulation area would arise due to the formation of ice layers by the refreezing of meltwater (Braithwaite et al, 1994). If the refreezing process causes impermeable layers at the surface, it would cause a migration of the runoff limit upslope, acting to further increase the mass loss due to runoff (Braithwaite et al, 1994). From 1978 to 1996, Drinkwater and Long (1998) detected an upslope migration of the percolation zone (area where melts occurs but refreezes within the annual snowpack) and reduction in extent of the dry snow zone on the Greenland Ice Sheet which coincided with an increased melt rate and a 1.0ºC atmospheric warming. Details of the various facies zones are described below.

Snow accumulation and surface melt patterns form up to five distinct facies zones on the surface of glaciers and ice caps (Figure 1.2) (Benson 1960; Muller 1962; Koerner 2005). The main characteristics of these facies are as follows:

1. The *glacier ice zone* is located below the equilibrium line altitude (ELA) in the ablation area, and forms where winter accumulation melts completely, exposing bare glacier ice.
2. The *superimposed ice zone* is located immediately above the ELA. Here, the winter snow pack melts completely, but the annual balance is positive as mass accumulates by the refreezing of meltwater on the glacier surface.
3. The *saturation zone* (also known as the 'slush zone') is located above the superimposed ice zone, separated by a boundary termed the 'firn line'. In the saturation zone, the winter snow pack does not melt completely, but the snow that does remain throughout the

summer is transformed into firn. Here, meltwater can penetrate below the last summer surface (LSS), eventually refreezing and resulting in internal accumulation (Koerner 2005). This causes problems when measuring annual mass balance as it is difficult to account for the amount of mass that refreezes internally and that which is lost by runoff. In an attempt to resolve this issue, a 'tray' technique has previously been used which collected meltwater in a tray placed at the LSS layer resulting in the mass from the following year to be retained in or above it (Koerner 1970). However, this technique has only been used sporadically since problems such as the trays overflowing would frequently occur.

4. The *percolation zone* is located above the saturation zone, separated from it by the 'saturation line' or 'slush limit'. Here, melt water refreezes within the annual surface layer causing the layer to increase in density.
5. The *dry snow zone* is located above the percolation zone at high elevations, where no melt occurs. At the present day, the dry snow zone is a temporally intermittent phenomenon in the upper parts of ice caps in the CAA (Wolken et al 2009).

A change in melt extent will influence the spatial distribution and net accumulation of these various facies (Benson 1960; Muller 1962; Boon et al 2010), and therefore the overall surface mass balance of the glacier. Glacier facies within the accumulation zone on Devon Ice Cap (DIC) have been the focus of numerous past studies due to the relationship between changes in facies zones and climate change (Benson 1961; Muller 1962; Koerner 1970; Koerner 2005). For example, from 1963 to 1988 the superimposed ice zone on DIC was most commonly found at an elevation of ~1000 m, whereas from 1989 onwards this facies zone was found at an elevation of

~1160 m (Colgan and Sharp 2008). The progression of these facies zones to higher elevations is indicative of an increase in surface melt and warmer summer temperatures.

The relationship between glacier facies and the runoff zone (area where mass can be lost by meltwater runoff) is seen in Figure 1.3. Braithwaite et al (1994), suggests that the division between the superimposed ice and the saturation zone (known as the 'firn line') is closely related to the runoff limit.

Remote sensing techniques using microwave imaging sensors have been attractive for monitoring glaciers since they can be used independently of solar illumination, and regardless of the atmospheric conditions, which is essential when studying high arctic regions that exhibit periods of the year with 24 hour darkness (Quincey and Luckman, 2009). Synthetic Aperture Radar (SAR) imagery, which is in the microwave part of the spectrum, can be used to distinguish and monitor glacier facies based on the differential backscatter from each facies zone. Also, the wide swath widths of many SAR sensors (e.g., 405 km for EnviSat ASAR Wide Swath mode) enable large areas, such as entire ice caps, to be monitored at once.

1.1 Thesis objective

The objective of this thesis is to assess the relative mass balance of DIC by monitoring the migration of the glacier facies zones across the ice cap between 2004 and 2011 using a combination of remote sensing and in situ measurements. GPR profiles, weather station data, and mass balance stakes on the northwest sector of DIC provide information on the extent of the various glacier facies and validate the accuracy of the remote sensing techniques. The change in glacier facies and the annual mass balance in the northwest sector from 2004 to 2011 are put into

larger context by comparing the recent changes to the long-term 1960-2011 mass balance record. Based on this, inferences can be made concerning the relative mass balance of DIC from 2004 to 2011 compared to the long-term trend.

1.2 Thesis Format

This thesis is presented in article format with a manuscript intended for publication in chapter 3. This article, 'Recent changes in glacier facies zonation on Devon Ice Cap, Nunavut, detected from SAR imagery and field validation methods' was written by Tyler de Jong and is intended on being submitted for publication, with Dr. Luke Copland and Dr. David Burgess as co-authors. Since this section is intended as a standalone publication, some of the information provided in the other chapters of the thesis is repeated in Chapter 3. Chapter 2 provides a background to the remote sensing methods in this study. The tables and figures are presented at the end of each chapter, with references listed at the end of the thesis. A conclusion chapter summarizes the main findings and places them in a wider context of other cryospheric changes currently being observed in the Arctic.

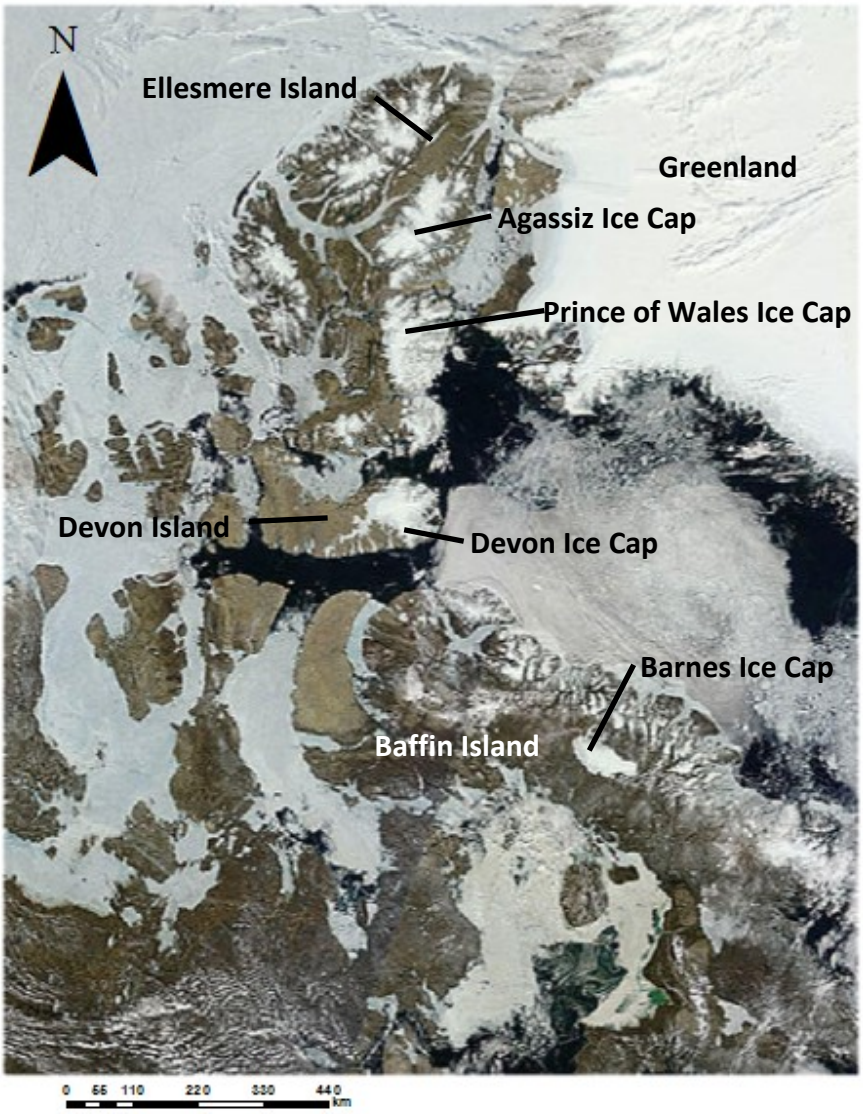

Figure 1.1 Mosaic from MODIS Terra (4km True Color 2011/07/05) showing the location of the main ice caps in the CAA

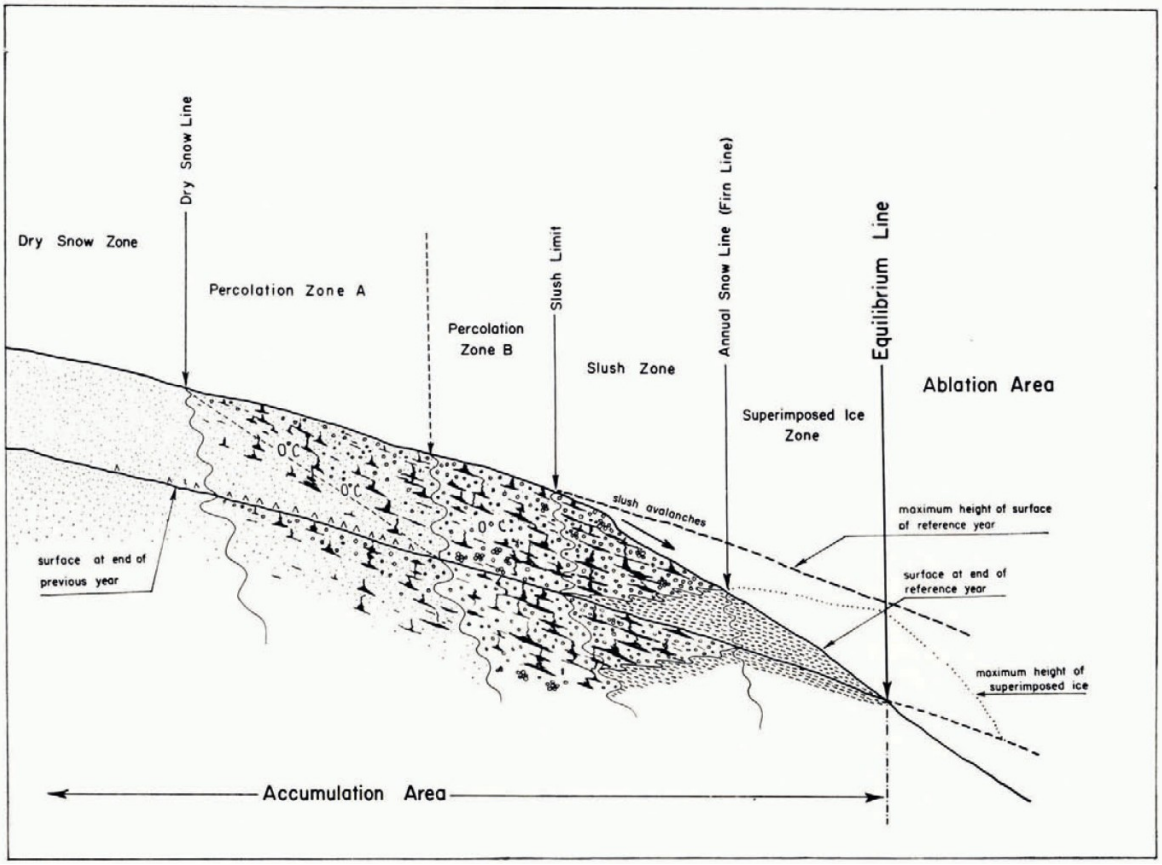

Figure 1.2 Illustration from Muller (1962) of typical glacier facies zonation on a polar ice cap

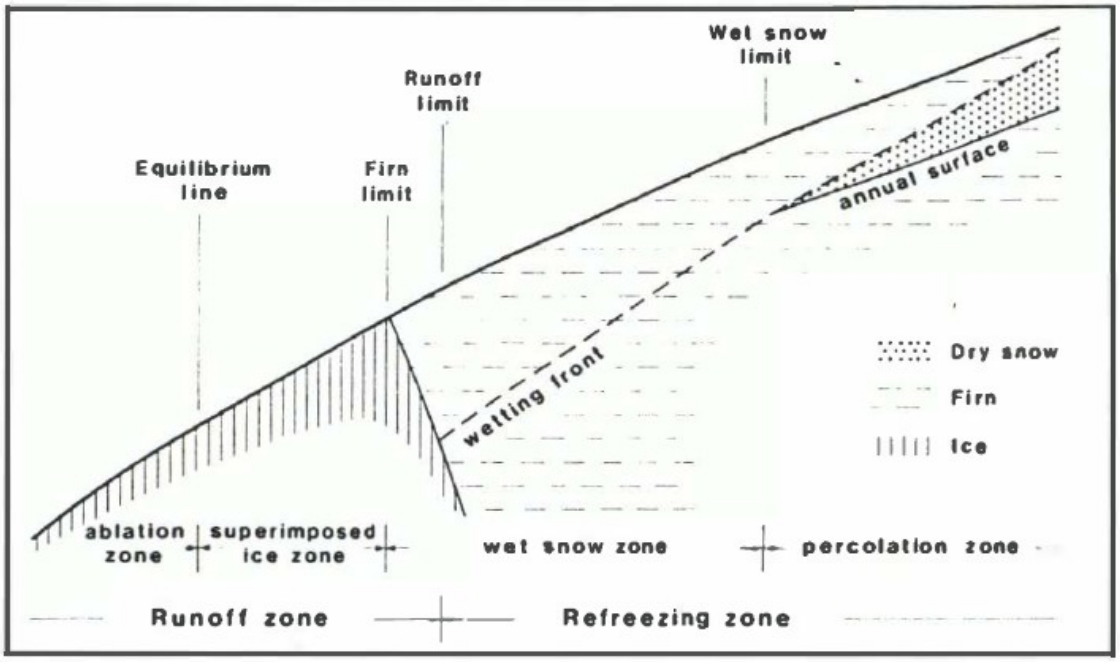

Figure 1.3 Illustration from Braithwaite et al (1994) depicting the location of the runoff and refreezing zones on a glacier

Chapter 2: Background to RADAR remote sensing

This chapter provides an overview of the principles of radar remote sensing, followed by a review of how the ground response to radar impacts the resulting radar image. The application of radar in the field of glaciology is described, with a particular focus on glacier facies identification.

2.1 Principles of RADAR

Radio Detection and Ranging (RADAR) describes an imaging active microwave sensor, meaning that it emits its own radiation. When mounted on a satellite platform, this radiation can be directed towards the Earth's surface and used as a source of illumination. As a result, radar imaging is independent from solar illumination and can be useful at high latitudes during the polar night, and regardless of most atmospheric conditions (Massom and Lubin, 2006). Radar emits pulses of microwaves which have wavelengths anywhere from 0.01 to 1 m (Figure 2.1). The radar antenna receives a fraction of the reflected signal from the Earth's surface, and the strength of this backscattered signal is recorded and used to distinguish targets with different surface characteristics (Figure 2.2). Additionally, the time delay between the emitted microwave and the portion of energy reflected back to the sensor can be recorded to determine the target's distance and location (CCRS, 2007).

There are multiple microwave bands, which refer to unique wavelength and frequency intervals shown in Figure 2.1. The wavelength and frequency are related by the formula:

$$c = \lambda v \qquad (1)$$

where c equals the speed of light, λ refers to the wavelength (m), and v refers to the frequency (cycles per second, Hz). Longer microwave wavelengths with lower frequencies can penetrate more easily through cloud cover, haze, dust, and snow cover than shorter wavelengths (Lillesand et al, 2008). However, shorter wavelengths are reflected by smaller features, thus providing more detailed information at small scales. For example, Ground Penetrating Radar (GPR) surveys at long wavelengths and low frequencies (~5-50 MHz) can detect the depth of a glacier bed below >1000 m of ice (Binder et al., 2009; Moorman and Michel, 2000), yet not be able to discern individual ice lenses in the near-surface snowpack. In this case, GPRs with shorter wavelengths and higher frequencies (~50-1000 MHz) can be used to detect small scale features such as ice lenses and shallow snow depths (Sylvestre, 2009; Palli et al, 2002). C-band (λ = 3.75-7.5 cm) and X-band (λ = 2.1-3.75 cm) sensors are therefore commonly used to detect surface changes (e.g. glacier facies) due to their shorter wavelengths and higher frequencies that are sensitive to small scale features (Casey and Kelly, 2010; Forster et al., 1996).

A microwave has two varying components: the electric and magnetic fields (Figure 2.3a) (Born and Wolf, 1999). The polarization of the microwave radiation refers to the orientation of the electrical field emitted and received by the radar sensor, and is comprised of a vertical and horizontal component (Figure 2.3b). The orientation of the electrical field is important since different polarizations will interact with the Earth's surface differently, thus affecting how the radar depicts the surface. There can be four combinations of polarizations (Figure 2.3b), with each providing different and complementary information about surface properties. Various radar sensors can transmit and receive one (e.g. Radarsat-1; ERS1/2), two (e.g. EnviSat), or all four (e.g. Radarsat-2; TerraSAR-X) of these combinations (CCRS, 2007; ESA 2013; CSA 2011). An example of how different polarizations and wavelengths can highlight different features in the

same scene is seen in Figure 2.4. Here, certain surfaces are brighter or darker according to their polarization since the relative phase of the returned wave differs from one polarization to another. Also, the L-Band imagery (1.25 GHz) penetrates deeper into the glacier than C-band (5.3 GHz) due to the larger wavelength, better revealing crevasses and a bergschrund (Konig et al., 2000). C-band, on the other hand, can identify surface conditions more easily, such as the location of the firn line.

The typical viewing geometry of a radar sensor is seen in Figure 2.5. Here, *A* refers to the flight direction, *B* refers to nadir (location on the Earth's surface directly beneath the platform; typically the shortest distance from the Earth's surface to the sensor), *C* is the swath width (width of the imaging surface), *D* refers to the range which is the across-track dimension perpendicular to the flight path, *E* refers to the azimuth which is the along-track dimension parallel to the flight direction, and *F* is the incidence angle which refers to the angle at which the radar 'looks' at the surface (CCRS, 2007). The side-looking platform is typical for virtually all airborne or spaceborne radar sensors. Due to their high flight altitude, spaceborne sensors can have a very large swath width (400+ km), making them useful to analyze large areas at once.

Synthetic Aperture Radar (SAR) comprises the most commonly used airborne and spaceborne radar sensor for imaging the Earth's surface. SAR uses a technique that simulates a large antenna length to achieve a uniform, fine azimuth resolution across the entire imaging swath (Figure 2.6). The motion of the SAR sensor is used to create an array of real antenna positions which are added together to simulate a larger antenna length (Elachi, 1987). The emitted beamwidth is inversely proportional to the antenna length (also termed 'aperture'), meaning that a longer simulated aperture length creates a narrower beam and finer resolution. In theory, the resolution

is half the antenna length, so for a 1 m antenna the resolution would be 0.5 m (Lillesand et al., 2008).

2.2 Ground response to radar

The ground response to radar is a function of the emitted wavelength, surface roughness, radar viewing and terrain geometry, electrical properties of the surface, polarization, and vertical structure of the surface (Bardel et al, 2002; Quincey and Luckman, 2009). Because of this, radar can be used to classify surfaces with different characteristics based on the intensity of backscatter (sigma nought, σ^0).

Surface roughness describes the size of surface features being imaged versus the wavelength of the SAR sensor being used. If surface features are substantially larger than the incoming wavelength, then the surface is described as being 'rough' and a significant portion of the radar signal will be reflected (Bardel et al, 2002). For example, if surface features are larger than 5.6 cm (C-band wavelength of EnviSat ASAR) then a relatively high degree of backscatter would be seen in the radar imagery (Figure 2.7). In sea ice studies, the surface roughness (and therefore intensity of backscatter) is commonly used to distinguish between first year ice and multiyear ice as first year ice is relatively smooth and has a specular reflection off its flat surface, which yields a low backscatter (Figure 2.7a; Figure 2.8). Conversely, multiyear ice tends to be fairly rough, resulting in a diffused reflection, which yields a high backscatter (Nolan et al., 2002; Onstott, 1992; Daida et al., 1996) (Figure 2.7c: Figure 2.8).

Radar viewing and terrain geometry will affect the reflected signal from the surface due to the sensor's incidence angle and look direction relative to the surface's aspect and slope. Here, the

smaller the returned incidence angle, the brighter the backscatter will appear (Figure 2.9a). Additionally, the surface slope and orientation to the sensor affects how the signal will penetrate surface layers such as snow and firn (Ulaby et al., 1986). Higher penetration depths will be seen in areas with lower incidence angles; for example, if position 2 and 3 in Figure 2.9a were firn facies, a greater penetration depth would be seen at position 2 due to more direct interaction (lower incidence angle) between the signal and the surface.

The penetration depth of the SAR signal is also dependent on the wavelength (as discussed above) and is an important factor to consider when analyzing backscatter imagery. For example, on the Greenland Ice Sheet, Matzler and Wegmuller (1987) found that SAR penetration depths with a C-Band wavelength reached ~9 m in dry firn and ~11 m in the percolation zone. However, most of the scatter was seen to occur in the upper 6 m of dry polar firn (Dall 2007). Alternatively, L-band penetration depths of ~11 m in cold polar firn were recorded on the Greenland Ice Sheet by Rignot et al. (2001).

Radar image distortions occur in the range direction as a result of the satellite viewing geometry (Figure 2.9b). Because radar measures the distance of features from the sensor by recording the two-way travel time between the signal transmission and reception, targets closer to the sensor in the range direction will appear compressed compared to features further away that will appear elongated. Figure 2.9b depicts two targets of the exact same size on the ground (A1 and B1) that would have different appearances in a radar image (A2 and B2) due to their different distances from the sensor in the range direction (CCRS, 2007). Here, A2 appears compressed in the returned signal compared to B2, since it is located at a closer distance to the sensor.

In areas influenced by topography, two geometric distortions can occur: foreshortening and layover (Figure 2.10; Figure 2.11). Foreshortening is a consequence of the radar signal reaching low elevations before reaching higher elevations. This results in the relative distance from the sensor to the high and low elevation points being shorter than the ground distance between these locations (Figure 2.10a; Figure 2.11). This results in hillsides and mountains appearing compressed. In Figure 2.10a, the A-B slope appears compressed in the returned radar signal ($A^{'}B^{'}$) since the radar's distance from point A and B is shorter than the true distance between the points. Maximum foreshortening occurs on slopes which are perpendicular to the radar beam (C to D in Figure 2.10a), as the returned signal will show the entire slope to be at the same position ($C^{'}D^{'}$). Conversely, layover is a consequence of the radar signal reaching areas of higher elevations before reaching lower lying areas (Figure 2.10b; Figure 2.11). Here, the high elevation areas will return a backscattered signal to the sensor before the low lying areas, thus making high elevation areas 'lay over', or be positioned in front of the low lying areas. As a result, the features in the range direction are displayed incorrectly. Both foreshortening and layover result in a shadow effect, preventing features being seen by the radar (Figure 2.10c; Figure 2.11). This occurs down range of vertical features, as a result of the inability of the radar signal to illuminate on the lee side of tall features. These shadow areas are displayed as dark surfaces in radar imagery as no incoming radar waves are able to be backscattered (CCRS 2007).

To get a true backscatter coefficient (sigma nought, σ^{o}) the SAR signal must be corrected for radar viewing and terrain geometry (Johnsen et al., 1995) (Figure 2.12). Units are generally described in Decibels (dB) and reflect a radiometrically calibrated surface. A DEM is generally used to correct for topography, and satellite orbital math models are used to correct for radar

viewing geometry (Johnsen et al., 1995). As a result, the quality of the corrected image is directly related to the quality of the DEM and satellite orbital math models.

Another contributor to the intensity of backscatter is the electrical properties of a surface which has an influence on the absorption, transmission, and reflection of microwave energy. The dielectric constant (relative permittivity) of a material is a measure of the electrical properties of a surface and is an indication of the reflectivity and conductivity of various materials (Lillesand et al., 2008). In a perfectly homogeneous dry snowpack, the magnitude of the radar backscatter is proportional to the dielectric constant, resulting in higher backscatter where the radar signal first interacts with a surface with a high dielectric constant. The stronger the dielectric contrast between two media, the stronger the backscatter is at the interface. However, wet snow is highly absorptive, meaning that the backscatter is very low and appears dark in a radar amplitude image (Massom and Lubin, 2006). Additionally, the dielectric constant of snow depends on the crystal shape and snow density, whereas the dielectric constant of ice is also temperature dependent (Glen and Paren 1975). The dielectric constant of snow increases as density increases according to the following equation:

$$\varepsilon' = 1 + 1.7\rho_{snow} + 0.7\rho^2_{snow} \quad (2)$$

where ε' is the dielectric constant and ρ_{snow} is the snow density (Tiuri et al., 1985). Since the electrical properties of snow are significantly altered by the presence of liquid water, the detection of melt is easily made with the use of SAR imagery (e.g., Casey and Kelly, 2010; Wang et al., 2007). At the onset of melt, the surface transitions from a reflective surface (bright backscatter) to an absorptive surface (dark backscatter). Dielectric absorption is dependent on temperature as increased absorption occurs near the melting point (Conway et al., 2009). Once

liquid water is present, the dielectric absorption of snow increases dramatically. By creating simple thresholds in σ^0 values, it is possible to map melt extent over large areas due to the large contrast in dielectric constants in dry versus wetted snow facies (Quincey and Luckman, 2009). An example of the typical melt progression identified with SAR imagery on Devon Ice Cap is seen in Figure 2.13.

Although the dielectric constant is important in terms its contribution to backscatter, the vertical structure of the near-surface can sometimes be more important in determining the strength and characteristics of reflections (Zahnen et al., 2002). For glaciers and ice caps, the vertical structure of the near-surface typically refers to snow/firn stratification and the distribution, size, and 3D distribution of elementary scatterers (e.g., ice lenses and pipes in glaciers). This also refers to the potential for *volume scattering*. Volume scattering describes what happens when scattering occurs from within snow and firn layers as individual grains and inhomogeneities at depth scatter some of the incoming energy in a diffused manner (Figure 2.14) (Bardel et al, 2002). High optical depths (depth at which a radar wave can penetrate into a surface) increases the potential for volume scattering, which would thereby enhance the amount of backscatter (Bardel et al, 2002). The reflection off multiple internal layers on glaciers (e.g. ice lenses) increases the total path length of the signal, thus enhancing the opportunity for volume scattering (Figure 2.14) (Ulaby et al, 1986). Overall, an inhomogeneous 3D distribution of elementary scatterers will increase the amount of volume scattering. In addition, since layers of different densities have different dielectric constants (Glen and Paren, 1975), more internal reflections occur due to an increase in scattering surfaces, thus enhancing the volume scattering. As a result, the percolation/saturation zone on a glacier will have a very high backscatter since it is comprised of

large grain sizes, multiple ice lenses and pipes, and an inhomogeneous surface which causes this zone to have very efficient scatterers.

2.3 Use of SAR to detect glacier facies

Previous studies have used SAR imagery to detect glacier facies zones based on backscatter classifications (e.g., Partington 1998; Engeset et al, 2002; Wolken et al, 2009). C-band and X-band wavelengths are typically used in studies of glacier facies since the backscatter at these wavelengths is influenced by the near-surface and has a relatively low penetration depth (<11 m). The following describes how σ^o varies between different facies zone and time of year:

1. Dry snow zone: perennially low backscatter is typical as the radar wave tends to penetrate the snow pack and be absorbed due to the lack of surface scatterers (e.g. ice lenses and pipes). This zone has a low density and low dielectric constant, thus causing little backscatter (Wang et al., 2007).
2. Percolation and saturation zones: these zones are difficult to distinguish through SAR, as their scatterers are similar (Casey and Kelly, 2010). Here, backscatter is high during the winter, since ice lenses and pipes act as effective scatterers. In summer, backscatter is lower since the wet snow absorbs much more of the incoming signal (Massom and Lubin, 2006).
3. Superimposed and glacier ice zones: backscatter is low once melt starts in the overlying snowpack, but then increases in late summer once bare ice (an efficient scatterer) is exposed. In winter, the homogeneous structure of superimposed and glacier ice does

not favour backscatter, leading to low backscatter values across this zone (Wolken et al., 2009; Bardel et al., 2002; Partington 1998)

The potential to classify various glacier facies zones with SAR imagery forms the basis of this thesis. Changes in glacier facies using autumn/winter Envisat ASAR imagery are monitored on Devon Ice Cap from 2004 to 2011 and validated with in situ GPR, temperature and mass balance data. The impacts on relative mass balance in terms of densification and runoff are also considered in response to a migration of the superimposed and glacier ice zones to higher elevations.

Table 2.1. Relationship of pure ice, soft new snow, granular snow and water with density and the estimated dielectric constant (Tiuri et al., 1984)

Material	Density ($g\ cm^{-3}$)	Dielectric constant (ε)
Pure ice	0.9	3.15
Soft new snow	0.13	1.2
Granular snow	0.4	1.8
Pure water	1	80

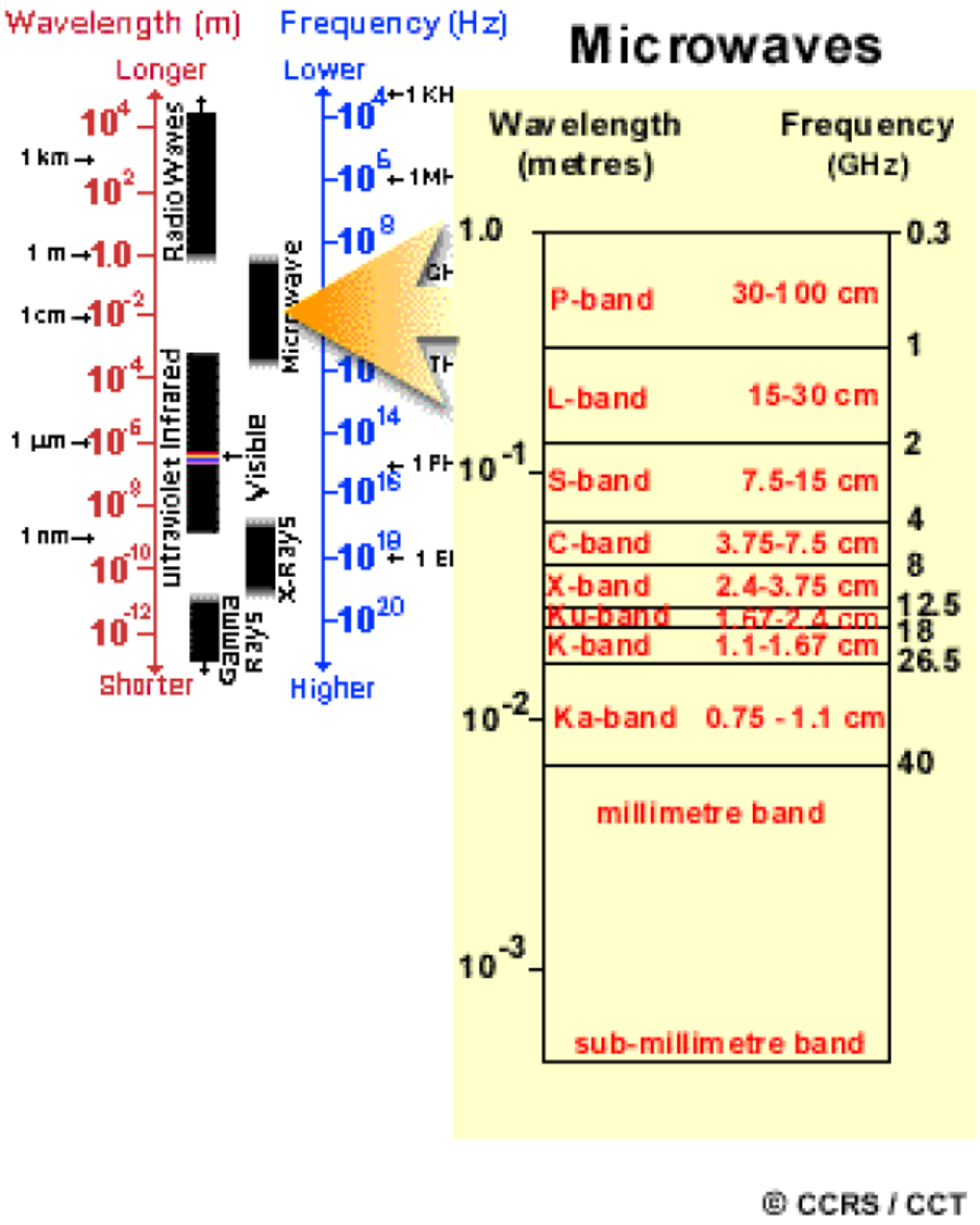

Figure 2.1 (a) Electromagnetic (EM) spectrum can be characterized by wavelength (m) and frequency (Hz). (b)The microwave portion of the spectrum (~1-100cm) can be defined according the classification bands seen here (CCRS, 2007)

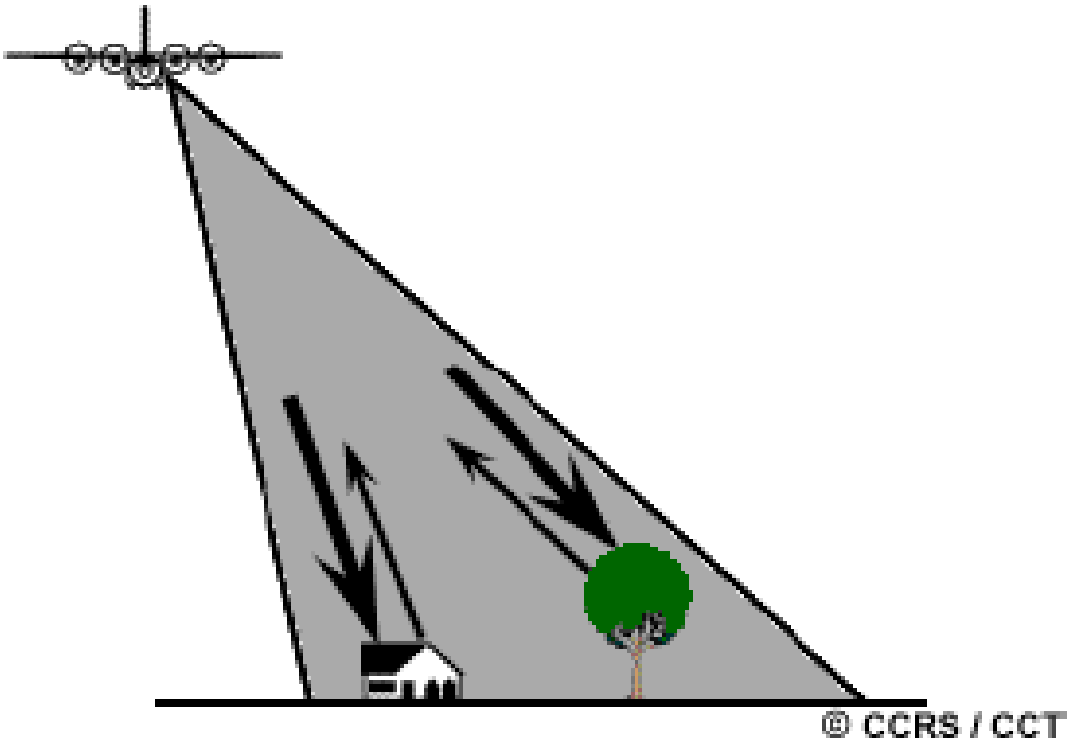

Figure 2.2. Radar sensor emits microwave radiation and records the strength of the returned backscatter (which is dependent on the targets characteristics) and two-way travel times between the transmission and reception of the signal (CCRS, 2007).

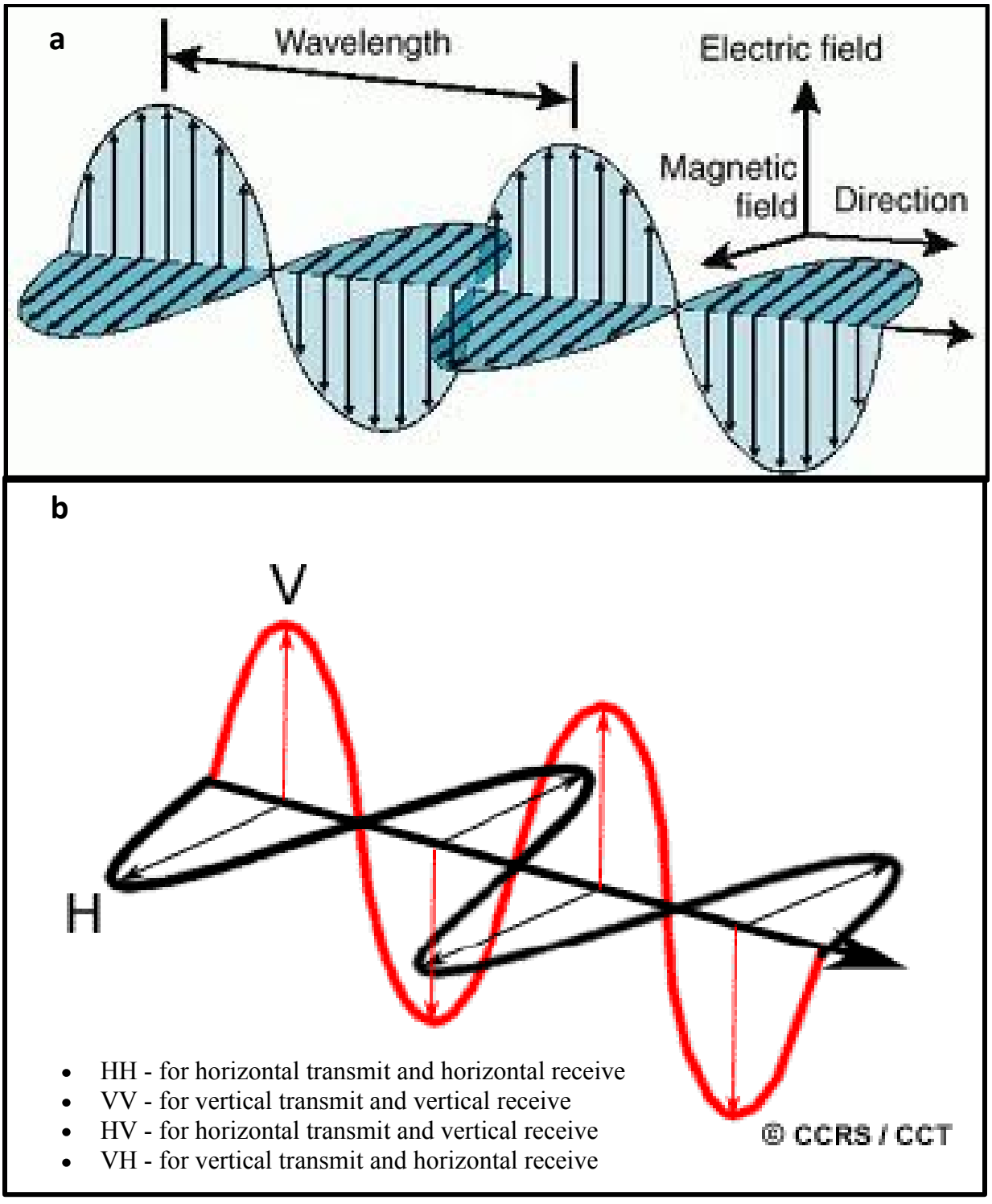

Figure 2.3. (a) Illustration of an electromagnetic wave showing the electric and magnetic field components. (b) The electric field itself has two polarizations (orientations): the Horizontal (H) and Vertical (V) components. Radar sensor can transmit and receive four combinations of polarizations; HH, VV, HV, and VH (CCRS, 2007).

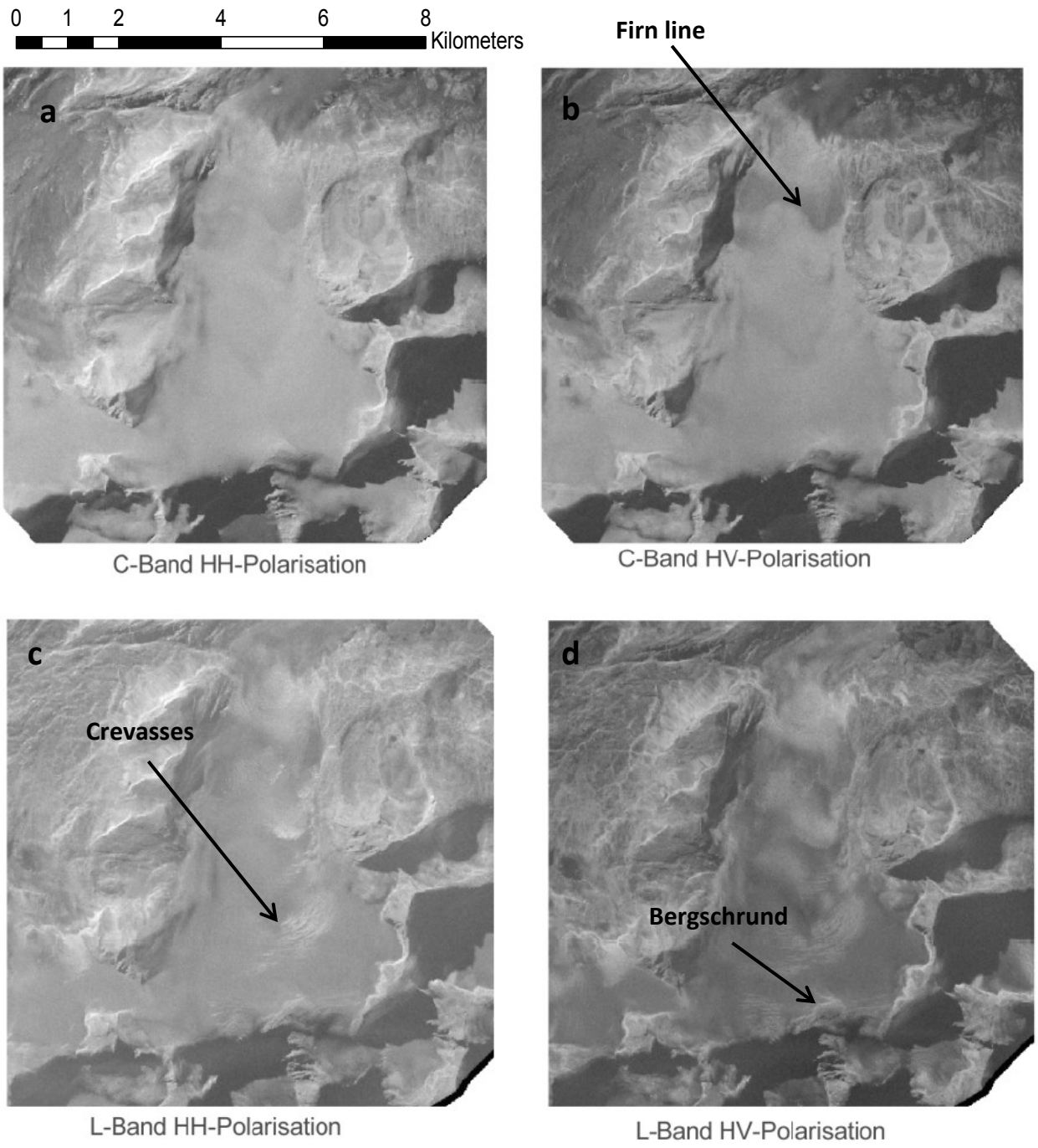

Figure 2.4 Airborne EMISAR images (20 m resolution) over Austre Okstindbreen, Norway, showing C-Band in HH and HV polarizations (a and b), and L-Band in HH and HV polarizations (c and d) March 23rd, 1995 (Konig et al., 2000)

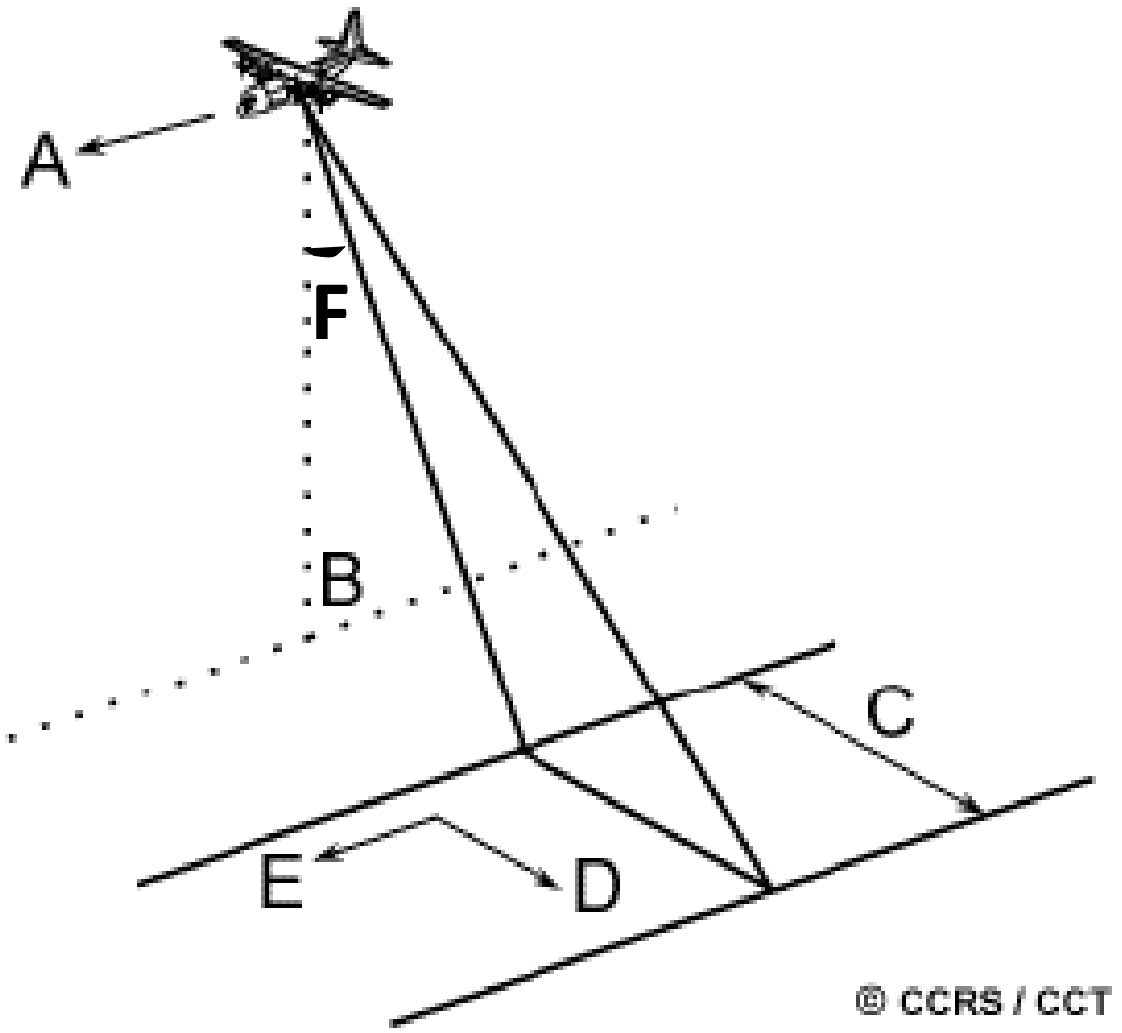

Figure 2.5. Typical side-looking radar viewing geometry. *A* is the flight direction, *B* is nadir, *C* is the swath width, *D* is the range direction, *E* is the azimuth direction, and *F* is the incidence angle (CCRS, 2007).

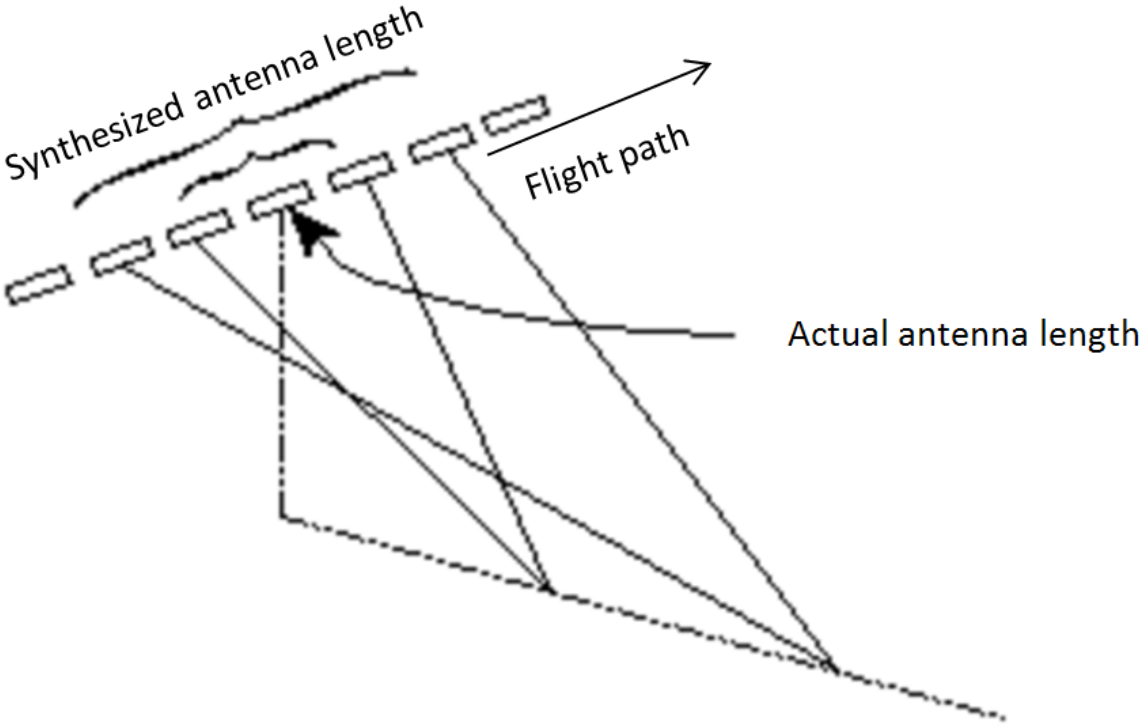

Figure 2.6. Example of how a SAR sensor creates an array of real antenna positions from the sensors motion to simulate a larger antenna length (Lillesand et al., 2008).

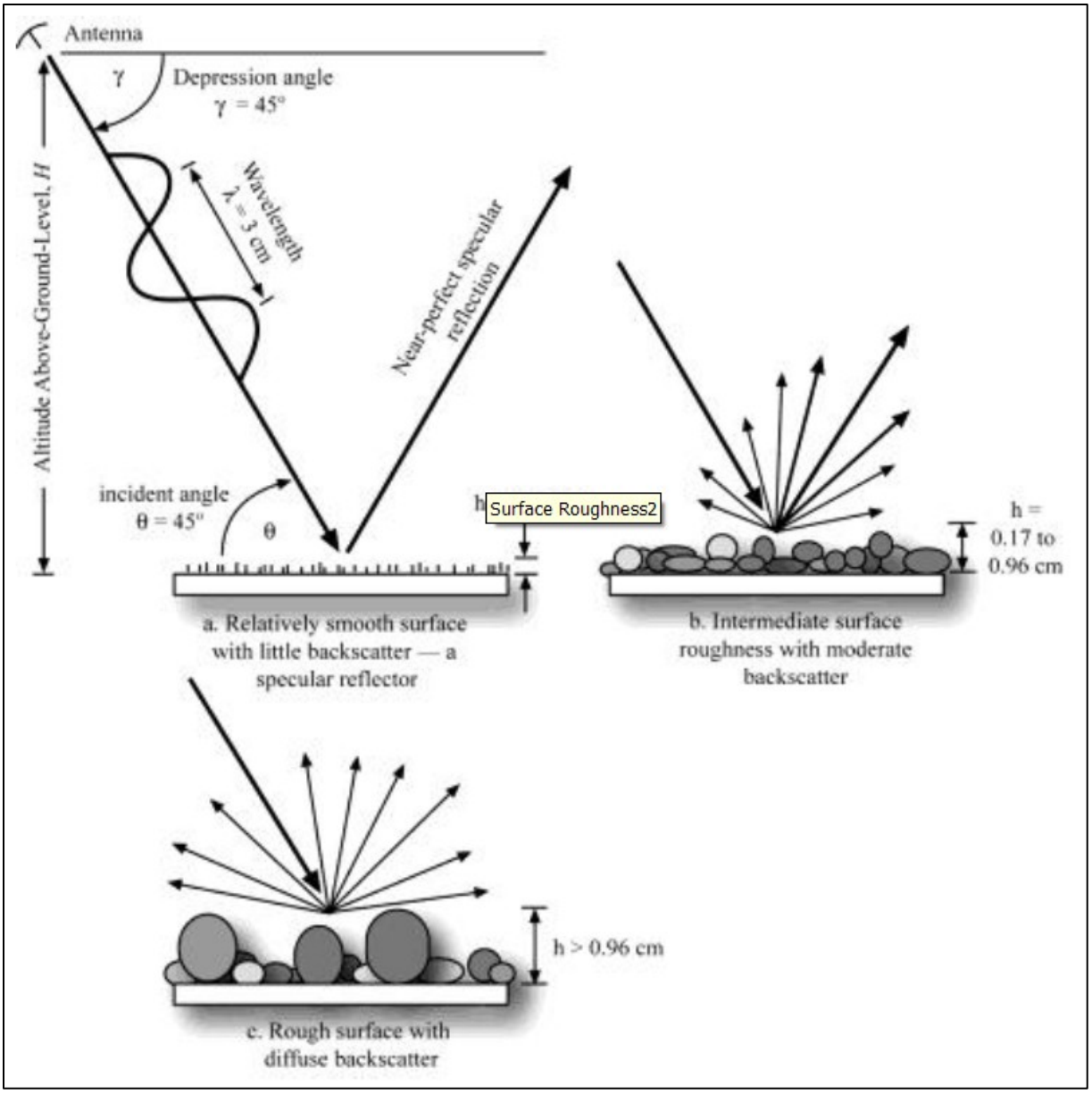

Figure 2.7. Differences between backscatter from surfaces with different surface roughness. A specular reflection (mirror-like) (a) is seen when the surface is fairly smooth, whereas more of a diffused reflection (b and c) is seen when surface roughness increases (source: A. Kaab, GEO9540 class notes)

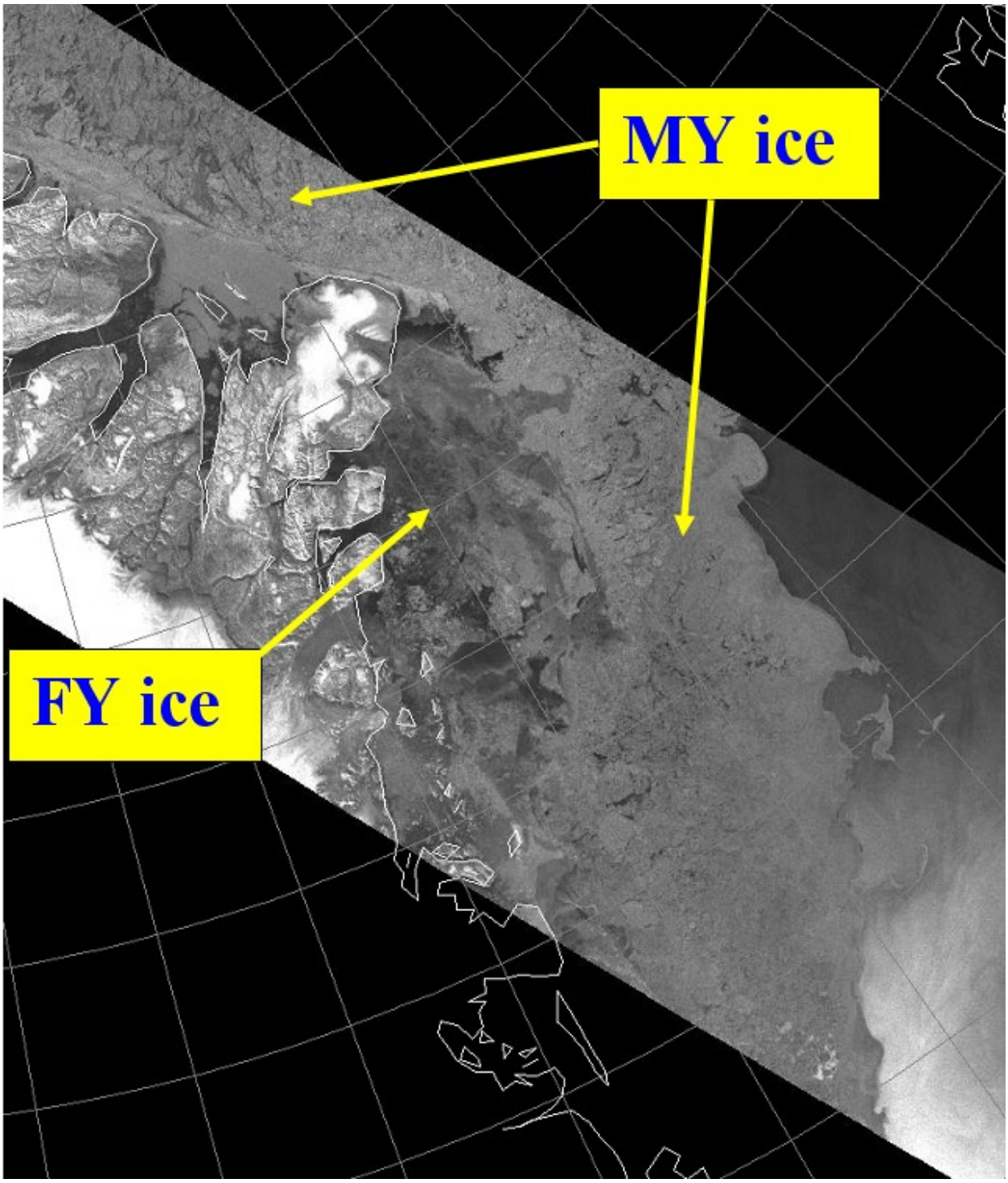

Figure 2.8 ENVISAT SAR image of the north east corner of Greenland on April 16, 2006. Note the difference between the lighter multiyear (MY) sea ice north of Greenland and the darker first year (FY) sea ice further south (source: galathea3.emu.dk)

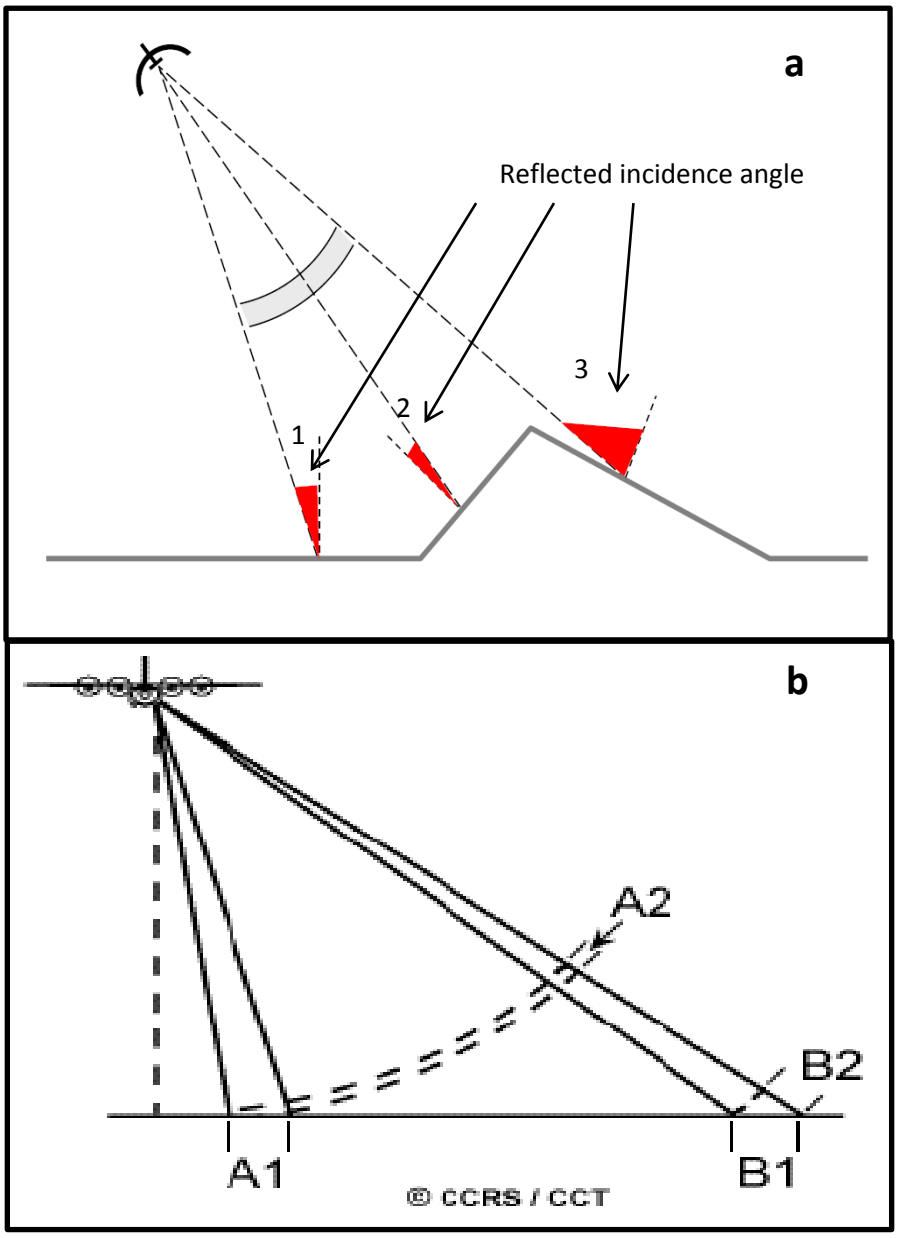

Figure 2.9. (a) Influence of the radar geometry and topography on the returned incidence angle. Higher backscatters are seen where the returned incidence angle is low (e.g., position 1 and 2 above) and a low backscatter where the returned incidence angle is high (e.g. position 3) (source: A. Kaab, GEO9540). (b) Radar image distortions in the range direction due to the different distance targets on the ground are to the sensor. The ground targets A1 and B1 are the same length in the range direction, however A1 appears compressed in the returned signal (A2) since it is closer to the sensor (CCRS, 2007).

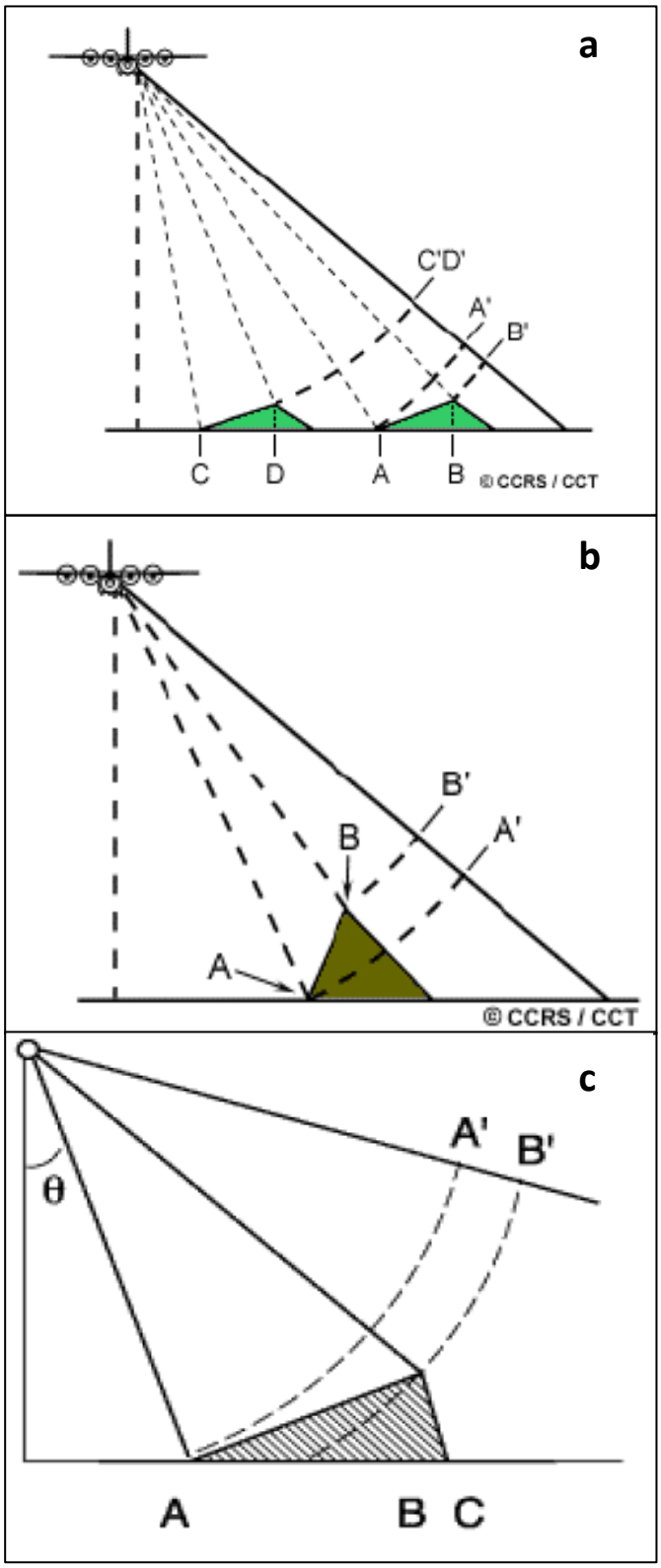

Figure 2.10. Illustrations showing the (a) foreshortening, (b) layover, and (c) shadow effects (CCRS, 2007)

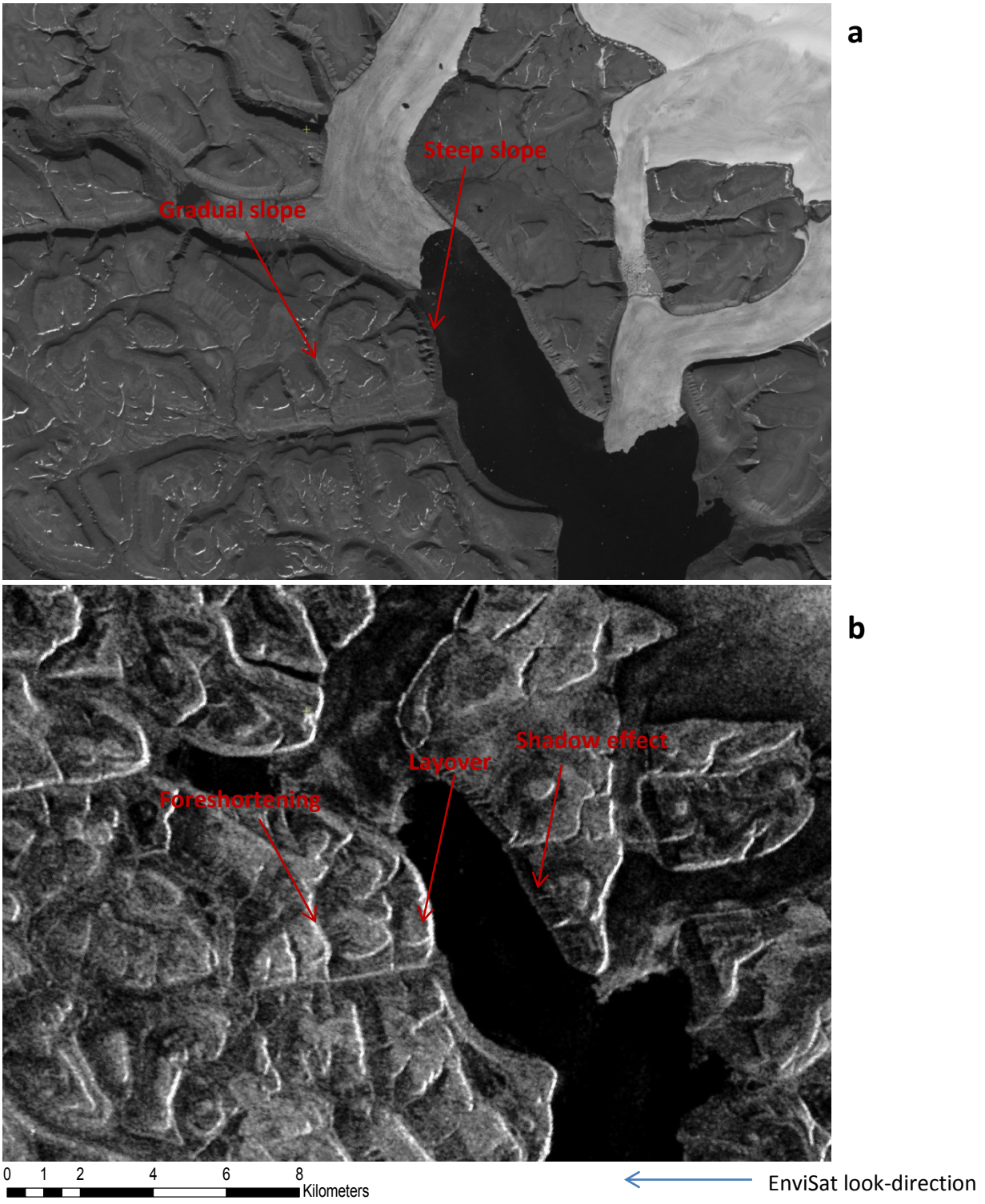

Figure 2.11. a) Panchromatic Landsat 7 image of the Croker Bay Glaciers, Southern DIC (July 7, 2000) with b) EnviSat ASAR WS image (November 17, 2011) showing foreshortening, layover, and shadow effects due to the ground and satellite viewing geometries.

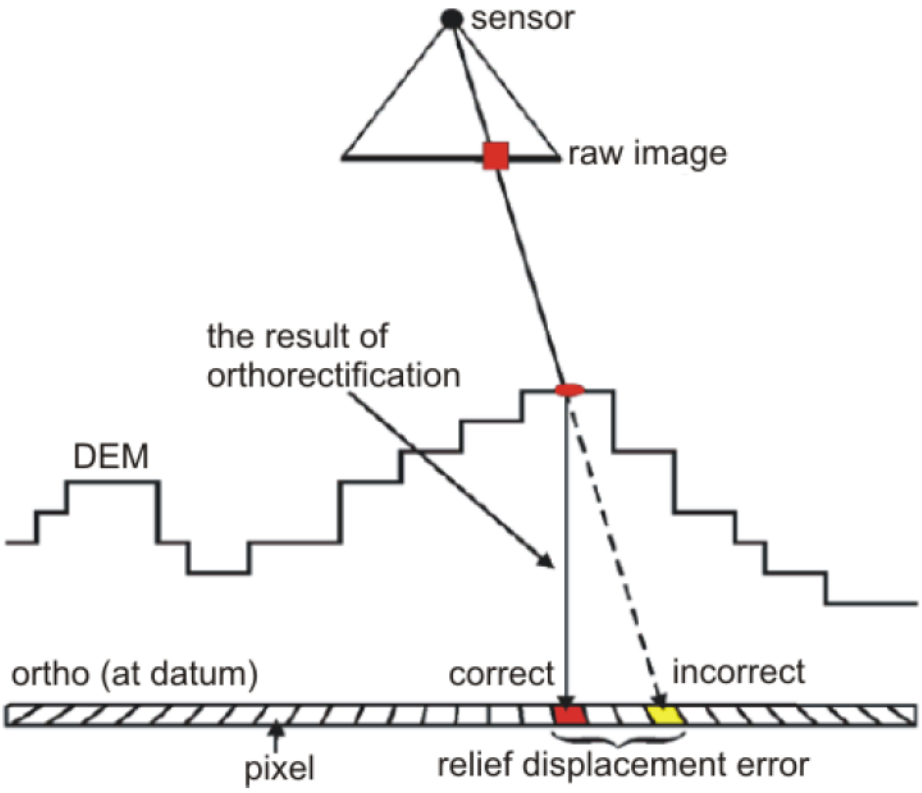

Figure 2.12. Depiction of the orthorectification method used to obtain a calibrated SAR backscatter coefficient which is corrected for incidence angles and topography (PCI Geomatica)

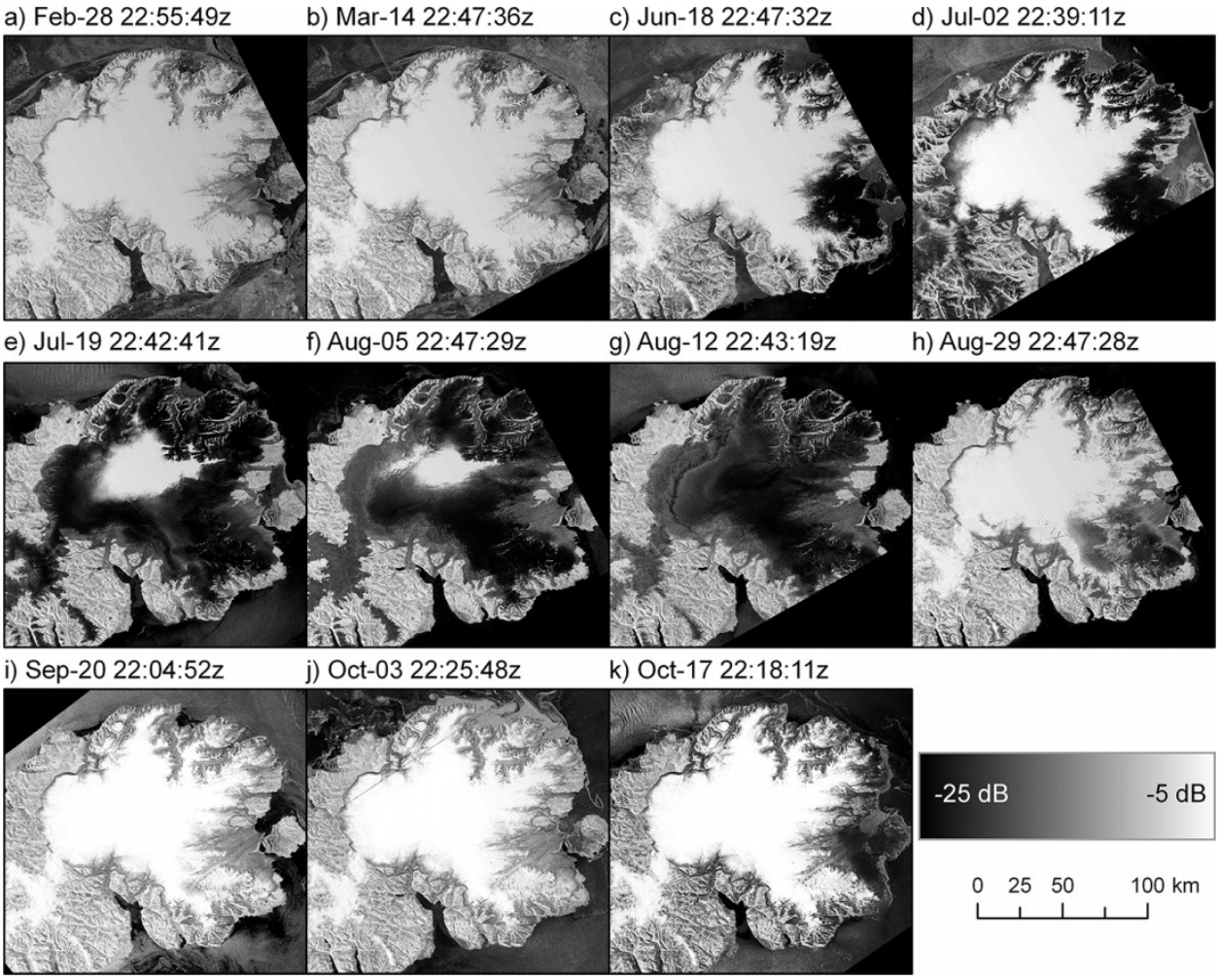

Figure 2.13. Radarsat-1 ScanSAR wide time series of DIC in 2006. Melt is first detectable on June 18th (c), becomes extensive in the summer months (d, e, f, g), and dissipates in the fall (Casey and Kelly, 2010).

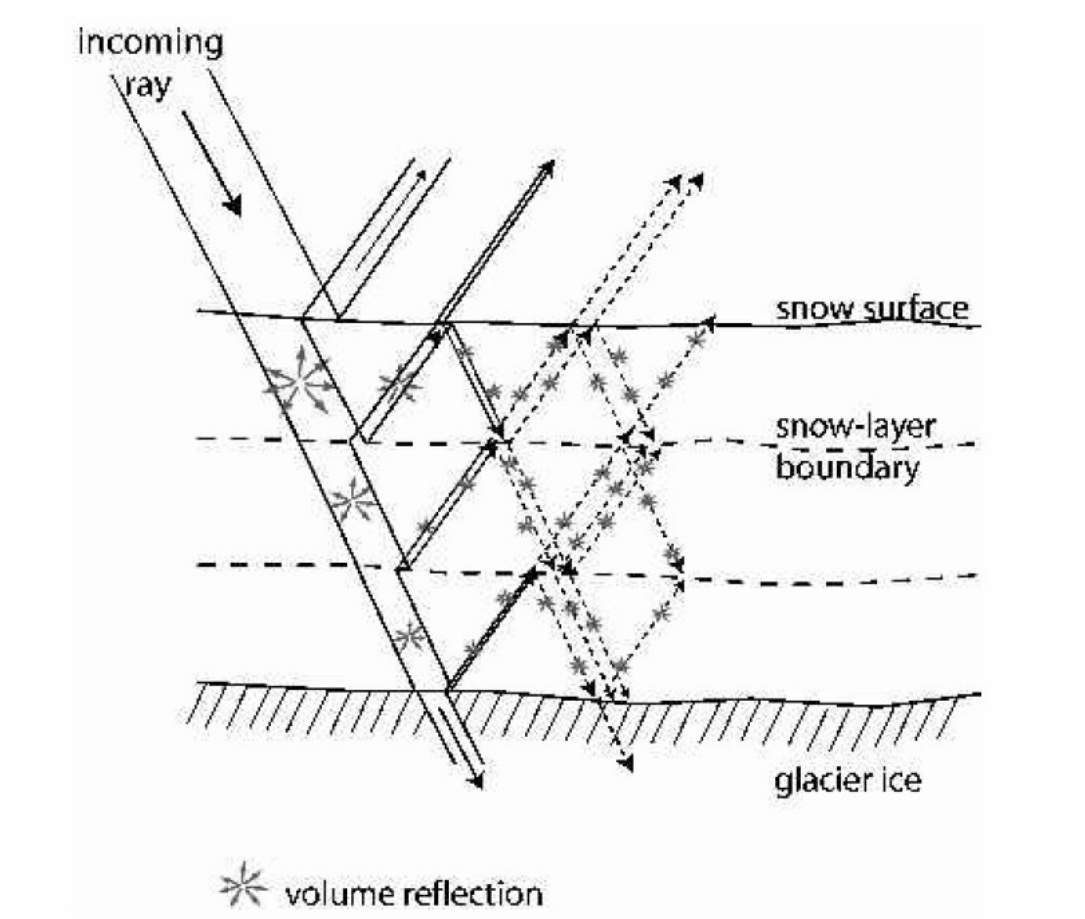

Figure 2.14. Reflection from volume scattering enhanced by the inhomogeneities and various layers of different densities within the snow pack (Bardel et al, 2002)

Figure 2.15. Image from Partington (1998) showing an ERS-1 SAR multi-temporal image mosaic of Greenland from 16 January 1993, 20 June 1992, and 29 August 1992. Dark regions indicate the dry zone snow zone and the bright region indicates the percolation zone (Partington, 1998)

Chapter 3: Recent changes in glacier facies zonation on Devon Ice Cap, Nunavut, detected from SAR imagery and field validation methods

3.1 Introduction

The Canadian Arctic Archipelago (CAA) contains the largest ice covered area outside of Greenland and Antarctica (Dyurgerov and Meier, 2005). Excluding the main ice sheets, the CAA represents approximately one third of total global ice volume (Radić and Hock, 2010). In recent years, glaciers and ice caps in the CAA have become a significant source of sea-level rise as anomalously high summer temperatures have caused an increase in summer melt (Gardner et al, 2011; Sharp et al, 2011; Fisher et al, 2012). Surface melt is estimated to account for ~92% of total mass loss from ice masses in the CAA, with iceberg calving accounting for most of the remainder (Gardner et al, 2011).

Gardner et al (2011) estimated glacier mass balance in the CAA from 2004 to 2009 using three different methods: (a) a comparison of inputs and outputs from surface mass-budget modeling (validated with *in situ* point surface mass balance measurements) and estimated iceberg calving rates, (b) determination of surface height changes with laser altimetry data from the Ice, Cloud and Land Satellite (ICESat), and (c) measurements of changes in mass derived from repeat passes from the Gravity Recovery and Climate Experience (GRACE) satellite. The results from the modeled surface mass balance plus iceberg calving showed a net mass loss of 34 +/-13 Gt a^{-1} in the northern CAA (north of Baffin Island) from 2004 to 2009. For the same time period, ICESat results showed a net mass loss in the northern CAA of 37 +/-7 Gt a^{-1}. Finally, GRACE measurements estimated a mass loss of 39 +/-9 Gt a^{-1} from 2004 to 2009 (Gardner et al, 2011). Limitations from the surface mass budget method include the relatively low spatial and temporal coverage of ground measurements across the CAA. In addition, repeat satellite laser altimetry does not examine the impact of internal accumulation and densification. Finally, the GRACE method has a low spatial resolution (~400 km), making it difficult to examine the mass balance of individual ice caps in the CAA.

Results from Jacob et al (2012) using GRACE measurements from January 2003 to December 2010 show that all glaciers and ice caps, excluding Greenland and Antarctica, have lost mass at a rate of 148 +/-30 Gt a^{-1}. In particular, results from the northern CAA (Ellesmere, Axel Heiberg,

and Devon Islands) showed a mass loss rate of 34 +/-6 Gt a^{-1} from 2003 to 2010. When including Baffin Island, the Canadian Arctic has the most negative mass balance rate (67 Gt a^{-1}) of all glaciers and ice caps outside of the main ice sheets (Jacob et al., 2012).

Sharp et al (2011) used *in situ* surface mass balance measurements from four glaciers (northwest Devon Ice Cap (DIC), Meighen Ice Cap, Melville South Ice Cap, and White Glacier, Axel Heiberg Island) in the CAA that have been measured annually since the early 1960s. Here, it was found that the four glaciers lost mass at an average rate of 493 kg m^{-2} a^{-1} (0.493 m w.e. a^{-1} when dividing by water density of 1000 kg m^{-2}) from 2005 to 2009, five times greater than the average 1963-2004 rate. This was largely attributed to the anomalously high summer temperatures during this period (Sharp et al, 2011).

Previous studies have found a strong relationship between mass balance and glacier facies zonation (Engeset et al., 2002). By looking at backscatter from Synthetic Aperture Radar (SAR) imagery, relative changes in mass balance have been inferred by examining the spatial distribution of glacier facies on an annual basis (e.g. Casey and Kelly, 2010; Engeset et al., 2002; Hall et al., 2000). With satellite swath widths able to cover large areas (e.g., 405 km for EnviSat ASAR Wide Swath mode), this enables the detection of changes in surface properties at an ice cap wide scale, and therefore monitoring of relative mass balance over large ice masses. For example, Casey and Kelly (2010) were able to distinguish between glacier ice, superimposed ice, and saturation/percolation zones on DIC, although they were not able to detect an apparent dry snow zone in 2004 using Radarsat-1 SAR data. Langley et al (2008) and Engeset et al (2002) used EnviSat ASAR and ERS 1/2 SAR imagery, respectively, to distinguish between firn and ice facies on Kongsvegen, Svalbard. The SAR-derived firn line (area where the surface transitions from ice to firn) and the equilibrium line altitude (ELA) were found to have a significant relationship (Engeset et al., 2002). In effect, since the location of the ELA is known to be an appropriate indicator of mass balance (Braithwaite, 1984), the location of the SAR-derived firn line can also be used as a proxy for detecting changes in relative mass balance.

The aim of this study is to determine recent changes in the mass balance of DIC from an analysis of temporal and spatial variability in the distribution of glacier facies. Facies zonation is initially mapped for the northwest sector of the ice cap using EnviSat ASAR data from 2004 to 2011, and validated against results from in situ Ground Penetrating Radar (GPR), temperature, and mass

balance data. Once validated, facies are mapped for the entire ice cap by extrapolating the ASAR methods to other sectors. This sheds light on how changes in the spatial distribution of glacier facies can have implications towards mass balance estimates, runoff rates and densification of ice caps.

3.2 Study Site

DIC is a polythermal ice cap located on Devon Island between 74º30'N to 74º50'N and 80º00'W to 86º00'W (Figure 3.1). It covers an area of approximately 14,400 km^2 (Burgess and Sharp 2004) and is one of the largest ice caps in the CAA. Airborne radar measurements over DIC were completed in 2000 by Dowdeswell et al (2004), who derived a maximum surface elevation of 1921 m, a maximum ice thickness of 880 m and an overall ice cap volume of 3980 km^3 (~10 mm sea-level rise equivalent). They also determined that 8% of the ice cap bed lies below sea-level and ~73 km (4%) of the ice cap margins end in tidewater.

DIC is located west of Baffin Bay, which provides its main moisture source from the North Open Water Polynya (Koerner 1966). The geography and hypsometry of the ice cap provide an important control on the spatial distribution of accumulation and ablation rates. For example, Mair et al (2005) found significantly different annual accumulation rates from ice cores drilled at similar elevations across the ice cap. Within the accumulation zone at an elevation of ~1330 m, annual accumulation rates from 1963-2000 varied from 267 kg m^{-2} a^{-1} in the southern sector to 127 kg m^{-2} a^{-1} in the northwestern sector (Mair et al 2005). This can be attributed to higher accumulation rates in the southeast due to its proximity to Baffin Bay and the erosive action of katabatic winds in the northwest (Koerner 1966).

Koerner (2005) showed that the annual mass balance of DIC from 1961 to 2003 was mostly negative. Cumulative balance in the northwest sector over this time was -3540 kg m^{-2}, with a mean annual mass balance of -82.25 kg m^{-2} (Koerner 2005). Additionally, from 1959 to 2000, a comparison of aerial photography and Landsat 7 ETM+ panchromatic imagery indicated that the ice cap decreased in area by 2.4% (332 km^2) (Burgess and Sharp 2004). This equates to a volume loss of 67 km^3 and a 0.17 mm contribution to sea-level rise. Most of the decrease in areal extent occurred from the eastern margin and stagnant southwest sector, while the western basin

experienced slight growth and the other areas showed no significant change (Burgess and Sharp 2004).

Results from Abdalati et al (2004), using airborne laser altimetry, showed that DIC thickened by 0.20 m a^{-1} at high elevations and thinned by 0.40 m a^{-1} at lower elevations between 1995 and 2000. However, Colgan and Sharp (2008) found anomalously low mean annual net accumulation from 1995 to 2000 from an analysis of shallow ice cores drilled at eight locations within the accumulation area. A potential explanation for this pattern is that neoglacial (Little Ice Age) cooling is only now reaching the bed, causing stiffening of basal ice and associated reduction in outflow from high elevations (Colgan and Sharp 2008). This cold neoglacial ice is less deformable and less prone to basal sliding, resulting in a near stagnant section of ice beneath the high elevations of DIC, which is causing the ice cap to thicken in these areas.

From 2005 to 2009, the mean annual mass balance of DIC was -341 kg m^{-2} a^{-1}, which was markedly more negative than the 2000-2004 mean of -198 kg m^{-2} a^{-1} (Sharp et al 2011; Koerner 2005). This has been attributed to anomalously warm summer temperatures and an increase in the length of the melt season during this time. Since 1963, 58% of the total mass loss from DIC has occurred from 2000 to 2009 (Figure 3.2) (Sharp et al 2011).

3.3 Glacier facies

Snow accumulation and surface melt patterns form up to five distinct facies zones on the surface of glaciers and ice caps (Figure 3.3) (Benson 1960; Muller 1962; Koerner 2005). Glacier facies are determined by the density, porosity, and permeability of the surface (Pfeffer et al, 1991), which produce unique reflectance characteristics that enable them to be identified in satellite imagery. The main characteristics of these facies are as follows:

1. The glacier ice zone comprises the ablation area, where total annual ablation exceeds total annual accumulation. Solid ice is exposed in this zone each summer as the winter snowpack completely melts away.

2. The superimposed ice zone is located immediately above the equilibrium line altitude (ELA). Here, the winter snow pack melts completely, but mass accumulates by the refreezing of meltwater on its surface, meaning that the annual balance is positive.

3. The saturation zone, also known as the 'slush zone', is located above the superimposed ice zone, separated by a boundary termed the 'firn line'. In the saturation zone the winter snow pack does not melt completely, with the snow that remains throughout the summer being transformed into firn. Here, meltwater can penetrate below the last summer surface (LSS), eventually refreezing and resulting in internal accumulation (Koerner 2005). This causes problems when measuring annual mass balance as it is difficult to account for the amount of mass that refreezes internally versus that which is lost by runoff.

4. The percolation zone is located above the saturation zone, separated by the 'saturation line' or 'slush limit'. Here, meltwater refreezes within the annual surface layer (and does not percolate beneath the LSS), causing the layer to increase in density.

5. The dry snow zone is located above the percolation zone at high elevations, where essentially no melt occurs. The presence of this zone requires very cold mean annual temperatures, meaning that it is typically only found in the interior parts of large ice caps and ice sheets.

Synthetic Aperture Radar (SAR) satellite imagery can be used to map different facies zones based on the intensity of backscatter (σ^o; sigma nought) of the SAR signal caused by the elementary scatterers on the glacier surface (Bardel et al, 2002; Engeset et al, 2002; Wolken et al, 2009). The dry snow zone has a perennially low backscatter as the radar wave tends to penetrate the snow pack and be absorbed due to the lack of surface scatterers (e.g., ice lenses and pipes), low snow density and small grain size (Wang et al, 2007; Partington 1998). Backscatter in this zone is relatively low compared with the surrounding percolation zone, yet greater than the glacier ice zone. The percolation and saturation zones are difficult to distinguish through SAR, as their scatterers are similar. Here, σ^o is the highest of any facies zone during the autumn/winter since ice lenses and pipes act as effective scatterers (Partington 1998). The glacier ice and superimposed ice zone have the lowest σ^o of all facies zones in autumn since the signal tends to penetrate ice to large depths (Hall et al., 2000) (Figure 3.4).

3.4 Methods

In this study, post freeze-up SAR imagery is used to monitor the spatial distribution of glacier facies across DIC, and is validated against *in situ* GPR, ice cores, mass balance and temperature data. The *in situ* surface mass balance was measured through a network of ablation stakes on the northwest sector of DIC (Figure 3.1), with temperature sensors on four of the ablation stakes used to calculate mean daily air temperatures. Finally, a GPR was towed across the ablation stake network from the upper accumulation area to the top of the ablation area to understand the near-surface snow and ice properties.

3.4.1 EnviSat ASAR imagery

Post freeze-up Envisat ASAR Wide Swath mode imagery was acquired for each year from 2004 to 2011 over DIC to observe glacier facies that developed as a function of the prevailing climate over the previous year (Table 3.1; Figure 3.5). All images were acquired from the European Space Agency's catalogue using the EOLISA ordering service (http://eoli.esa.int) and were provided in EnviSat ASAR level 1 format (.N1). EnviSat ASAR level 1 images are geolocated and corrected for distortions in the raw satellite imagery. The imagery was typically acquired in the fall, during periods of below freezing temperatures, when the absence of melt prevents the SAR signal strength from being affected by liquid water at or near the ice cap surface.

In areas where the LSS layer comprises an ice facies, the backscatter at the winter snow – ice interface dominates (Engeset et al, 2002). The presence of fresh dry snow above the LSS has a negligible impact on the reflected signal due to its low density and small crystal structure (Wang et al, 2007). Within the firn area (area above the superimposed ice zone) most of the scattering appears to be at the winter snow – LSS interface, as well as within the upper 6 - 11 m of firn in the form of volume scattering (Davies and Poznyak 1993). Volume scattering occurs when the individual grains and inhomogeneities below the winter snowpack scatter the incoming energy (Bardel et al, 2002). Where volume scattering occurs, a brighter reflection is seen since the reflection off multiple internal layers and ice features (e.g., ice pipes) increases the total path length of the SAR signal and enhances the opportunity for scattering (Ulaby et al, 1986). Past studies have suggested that C-band SAR penetration can be as much as 9 m in dry firn and 11 m in the percolation zone (Brown 2012). Nonetheless, within the accumulation area, changes at the

air-surface interface will show relative changes in annual backscatter, yet a degree of the backscatter is assumed to be due to the underlying layers. In the glacier ice zone, most scattering occurs at the air-surface interface, and volume scattering is assumed to be absent due to the uniformity and large SAR signal penetration depths within glacier ice (Forster et al 1999).

By analyzing EnviSat ASAR imagery with the *in situ* GPR and ice core data, initial identification of radar backscatter zones was undertaken in an attempt to classify different glacier facies based on the following principles (Figure 3.4):

1. The glacier ice/superimposed ice zone will have a lower backscatter and be at a relatively lower elevation than the saturation/percolation zone;
2. The saturation/percolation zone will have a higher backscatter and be at an elevation above the glacier ice/superimposed ice zone;
3. The dry snow zone will be located at the highest elevations and have a lower backscatter than the surrounding percolation zone;
4. The firn line is identifiable as the location with the highest contrast in backscatter between the glacier/superimposed ice and saturation/percolation zones

EnviSat Wide Swath mode, which has a resolution of 150 m and is in C-band ($\lambda = 5.6$ cm), was chosen as it enables a complete view of DIC at once and is able to detect surface features due to its relatively low wavelength. All EnviSat images were acquired from descending passes, and most of them (7 of 8) were from the same track number with a similar scene center, to keep the incidence angles consistent between acquisitions. This ensured that the changes seen in the imagery from 2004 to 2011 were due to real physical changes on the ice cap surface and not due to changes in satellite viewing geometry. The 2011 image has a different track number, although the scene center was very close to the other images. All images are in HH polarization (Table 3.1). Two 2008 post freeze-up images (10/2/2008 and 12/11/2008) with the same incidence angles were compared to evaluate change in the SAR backscatter throughout winter (Figure 3.6). Extracted sigma nought along the NW transect was within 0.15 dB in both images, thus showing that change in winter backscatter is fairly negligible.

Each image was orthorectified in PCI Geomatica's OrthoEngine, where a rigorous math model and a digital elevation model (DEM) were used to correct distortions due to variable viewing geometry and surface topography. In this study, a Canadian Digital Elevation Dataset (CDED)

DEM with a resolution of 50 m was used. The process within OrthoEngine uses the satellite position and orientation information to orthorectify each scene. The quality of the orthorectified images are dependent on the math model used by PCI Geomatica and the CDED DEM resolution. The resulting orthorectified images are radiometrically calibrated in sigma nought units (dB), and were used for the backscatter analysis. The output pixel spacing was 12.5 x 12.5 m and all images were projected in WGS84 UTM zone 17N.

The images were imported into ArcMap 10.0, where the σ^0 values were extracted at each pixel and averaged for each 50 m elevation band along two transects across DIC. The main focus of this study is along a transect in the northwest sector of DIC where near surface air temperature, GPR, and surface mass balance data were collected (Figure 3.1). In addition, a series of transects to the northeast surveyed with a GPR in 2008 by Sylvestre (2009) are used to validate the EnviSat ASAR backscatter values at a different location on DIC. More information about the air temperature, GPR and mass balance data collection methods is provided in the following sections.

3.4.2 Near surface air temperatures

Near surface air temperatures were measured at four automatic weather stations (AWS) at elevations of 1317 m (Ice Cap Station, ICS), 1594 m (Dev7D), 1731 m (Dev3F), and 1781 m (Dev1H) (Figure 3.1). The AWS were equipped with a Campbell Scientific 107F model thermistor with an accuracy of +/- 0.4ºC, and temperatures were recorded once a minute and averaged into daily values. The thermistors were positioned 1.5 – 2 m above the surface and kept in a Gill screen to protect them from direct incoming radiation. The mean daily temperature values were used to calculate the annual number of positive degree days (PDD) and freezing degree days (FDD) between 2004 and 2011 at each AWS. PDDs were calculated as the sum of all mean daily air temperatures above 0ºC, and FDDs were calculated as the sum of all mean daily temperatures below 0ºC. Mean seasonal temperatures were also calculated to assess if any seasonal trends influence the spatial extent of glacier facies. This data is compared with the backscatter values to assess the influence of near surface air temperatures on glacier facies across the surface of DIC.

3.4.3 Ground-penetrating radar

In May 2011 and 2012 a 450 MHz Sensors and Software pulseEKKO 1000 GPR system was towed behind a snowmobile across the northwest transect to map the facies zones within the accumulation area (Figure 3.1). The GPR was programmed to a time window of 160 ns, a stack size of 16, and a sample interval of 0.2 ns. Traces were recorded at a 1 second interval, which equates to a distance of 1.9 m at an average travel speed of 7 km hr^{-1}. An AshTech dual frequency GPS operating in kinematic mode, also recording at one second intervals, was used to provide position information for each GPR trace. Post processing of GPS data (to approximately +/- 10 cm in x,y,z) was completed through NRCan's Precise Point Positioning service (http://www.geod.nrcan.gc.ca/products-produits/ppp_e.php), which eliminated the need for a base station. Position estimates were provided based on the CSRS standard North American Datum of 1983 (NAD83).

The GPR data was edited and post-processed in pulseEKKO Deluxe software. A Dewow filter and SEC gain were applied to remove low frequency noise and amplify the signal at depth. In addition, a background subtraction (running average of 7 traces) was applied to remove repeated reflections resulting from 'ringing' of the GPR signal, and to highlight rapidly changing layers (Figure A2). In addition, the return from the winter snow pack was removed so that to the y-axis on the radargram commenced at the LSS. To acquire the radar wave velocity through firn in the accumulation area, the ice core density (ρ) at Dev1H (550 kg m^{-3}) was used to determine a dielectric constant (ε'_r) of 2.16 using the relationship from Kovacs et al. (1995):

$$\varepsilon'_r = (1 + 0.851\rho)^2 \qquad (1)$$

From this dielectric constant, a radar wave velocity (V) of 0.20 m ns^{-1} was found using the following equation:

$$V = c/\sqrt{\varepsilon'_r} \qquad (2)$$

where c is the speed of light (0.3 m ns^{-1}). As a result, the depth axis on the radargram was determined based on a radar wave velocity of 0.20 m ns^{-1}.

3.4.4 Ice cores

To validate the GPR measurements, ice cores were extracted at 1781 m, 1731 m and 1557 m (Dev1H, Dev3F and Dev8K, respectively, on Figure 1) along the Northwest transect in both May 2011 and 2012. Coring was completed with a Kovacs Mark II system, which retrieved cores with a 9 cm diameter. The Dev1H core had a length of 5.21 m in 2011 and 6.00 m in 2012, the Dev3F core had a length of 5.20 m in 2011 and 5.16 m in 2012, and the Dev8K core had a length of 3.82 m in 2011 and 4.52 m in 2012. The ice core stratigraphy was first recorded, and then the core was split into sections based on the boundaries between firn and ice layers. Subsequently, each section was weighed to calculate density. Locations of the cores were identified on the associated GPR radargram and used to distinguish firn and ice layers (Figure 3.7a).

3.4.5 Mass balance

A network of ~48 mass balance stakes located in the northwest sector of DIC has been measured annually each spring from 1961 to present (Figure 3.1). The difference in stake height above the LSS in two consecutive years is used to derive the net balance for a given year (δ mass balance stake height). The difference between the net annual balance and previous year's winter balance (snow depth measured in the spring) is then used to derive the summer balance (i.e. surface melt). The ELA is defined for each year as the location along the mass balance stake network where the annual balances transition from negative to positive.

To provide mass balance in terms of snow water equivalent (SWE), snow pack density measurements were taken throughout the northwest transect at every second stake. Snow pack densities above the LSS were determined by weighing a snow sample with a cylinder shaped probe with a known volume (1075.66 cm^3) that extracted an integrated sample to a depth of 60 cm below the surface, and then dividing the mass by the volume.

3.5 Distinguishing glacier facies zones

When comparing the GPR radargram with the ice cores taken at 1557 m (Dev8K) and 1781 m (Dev1H), ice and firn facies were able to be distinguished respectively (Figure 3.7a). Within the firn area the radar signal was highly scattered, producing a speckle pattern in the radargram.

Conversely, within superimposed and glacier ice areas the radar signal penetrated the ice with minimal scatter, resulting in clear areas in the radargram. The surface transition from ice to firn (firn line) was clearly distinguished in both the 2011 and 2012 radargrams (Figure A2). When the GPR results were plotted over the winter EnviSat ASAR imagery, the location of the LSS firn line on the GPR radargram occurred at the same location as the 0 dB contour and a zone of high backscatter contrast in the satellite image (Figure 3.7c). Thus, the EnviSat ASAR imagery was used to delineate the firn line at 0 dB (termed the 'EnviSat firn line'), and distinguish between the glacier ice/superimposed ice zone where backscatter was <0 dB, and the percolation/saturation zone where it was >0 dB.

To validate this method in another sector of DIC, work completed by Sylvestre (2009) to detect the firn line in the northeast sector was used for comparison (Figure 1). Similar to the current study, Sylvestre (2009) used a pulseEKKO Pro 500 MHz GPR to identify the 2007 firn line by tracking ice layers emerging at the surface. His results showed the firn line to be located between 1260 – 1300 m, which compares well with the northeast sector's EnviSat firn line of 1250 – 1300 m derived from the location of the 0 dB σ^o contour in the 2007 ASAR imagery (Figure A1).

In other studies, distinctions between superimposed ice and glacier ice zones using SAR backscatter values have been reported by Konig et al (2002) and Marshall et al (1995) based on regions of differing surface roughness and air-bubble content in the ice. However, in this study a distinction between superimposed and glacier ice to delineate an ELA could not be determined by SAR imagery alone. Instead, since an *in situ* ELA was known at a specific point along the northwest transect from the mass balance stake measurements, the σ^o value was extracted from this point and used to delineate an 'equilibrium line' (EL) based on backscatter and not elevation. Values below the σ^o EL were categorized as the glacier ice zone, and values between the EL and the firn line were categorized as the superimposed ice zone. It should be noted that superimposed ice can be present below the *in situ* ELA, however in this case the ice is categorized as glacier ice in the EnviSat imagery.

Casey and Kelly (2010) reported a dry snow zone on DIC in 2004, however were not able to detect it using Radarsat-1 SAR imagery. Melt occurred within this region in 2004 as some maximum daily summer temperatures were above 0ºC (David Burgess, personal communication), thus eliminating it from the true definition of a dry snow zone by Benson

(1960). For this reason the term 'pseudo dry snow zone' is used in this study to describe areas near the summit with minimal melt. In 2004, a lack of melt features acting as surface scatterers likely caused low backscatter at elevations >1300 m in the EnviSat ASAR imagery (Figure 3.5). AWS records indicated that no PDDs occurred at Dev1H (1781 m) or Dev3F (1731 m) that year, and only 4ºC of PDDs occurred at ICS (1317 m) (Figure 3.7). In addition, positive summer mass balances were seen at elevations down to 1317 m along the mass balance stake network in 2004, and the *in situ* measured ELA was recorded at 1090 m. Also, in August 2004, remnants of the previous winter's snowpack were seen at elevations of ~700 m in the southern sector (D. Burgess, personal communication). In effect, the low backscatter values seen in the 2004 post freeze-up ASAR imagery (Figure 3.5) across all elevations of the southern portion of DIC is likely due to the pseudo dry snow zone extending to the glacier/superimposed ice zone, making the division between these two zones indistinguishable.

In years with an extensive pseudo dry snow zone such as 2004, the LSS can be virtually transparent where little or no melt occurred. In effect, the summer surface from the year before is depicted in the SAR image due to the lack of surface scatterers and low density in the LSS. For example, the firn line in the 2004 imagery likely indicates the 2003 firn line, since the LSS in 2004 was virtually transparent due to the low melt rates which occurred at elevations >1300 m. Since a large portion of DIC in 2004 was covered by the pseudo dry snow zone, the 2004 results were not used to distinguish glacier facies extents for that year.

Zones of low backscatter values (dB < 0) in 2005 and 2006 (Figure 3.5) near the ice cap summit are also defined as the pseudo dry snow zone as data from the AWS at 1781 m (Dev1H) indicate that summer PDDs were 1ºC in 2005 and 7ºC in 2006 (Figure 3.8b). 2005 experienced the coldest winter (December-January-February) temperatures out of the 2004-2011 AWS records at ICS and Dev1H (Figure 3.9b). Cold winters can delay the onset of melt as more energy is required to raise the surface temperature to the melting point (Copland et al., 2007). The low surface melt would result in the presence of a relatively low number of surface scatterers such as ice lenses, and lead to low backscatter values indicative of a pseudo dry snow zone. Here, the low backscatter at high elevations of DIC from 2004 to 2006 (Figure 3.5) is likely due to the large penetration depth of the ASAR signal (Hall et al., 2000).

3.6 Results

3.6.1 Migration of firn line and area change of glacier facies from 2005 to 2011

Once the firn line and different glacier facies had been validated against the ground measurements, the firn line's location and total extent of each glacier facies across DIC was calculated for each of the EnviSat scenes from 2005 to 2011. Over this time, the EnviSat firn line increased in elevation on the northwest transect from 1555 m to 1685 m. This equates to a rate of 27 m a^{-1}, compared to a rise in the *in situ* derived ELA of 44 m a^{-1} over the same period (Figure 3.10).

From 2004 to 2006 at lower elevations (1300-1350 m) along the northwest transect, σ^0 increased from -2.2 to -1.4 dB. This is seen alongside an increase in PDDs (Figure 3.11a) and a decrease in the δ mass balance stake height at 1317 m from 0.20 to 0.06 m (Figure 3.11b). A subsequent decrease in σ^0 (-1.4 to -2.1 dB) occurred from 2006 to 2009 as the surface mass balance became negative at this location (Figure 3.10b). This trend in backscatter is indicative of an increase in surface scatterers (e.g., ice lenses and pipes) from 2004 to 2006, followed by a decrease in surface scatterers as this region became part of the superimposed and glacier ice zone. The 2004 – 2011 seasonal temperature trends at ICS indicate a gradual increase in winter and summer temperatures alongside no apparent trend in spring and autumn temperatures. The annual trend increased by 0.16ºC a^{-1} over this period (Figure 3.9a). Freezing degree days also increased since 2004, with two main peaks in 2006 (-5847ºC) and 2010 (-5744ºC) (Figure 3.8a).

The glacier ice zone generally increased in both area and maximum elevation from 2004 to 2011, with large advances in 2005, 2008, and 2011. In 2005, the glacier ice zone occupied 71% (10,282 km^2) of the entire ice cap. This zone increased to 85% (12,189 km^2) and 90% (12,971 km^2) of the total ice cap area in 2008 and 2011, respectively (Figure 3.12).

From 2005 to 2007, the percolation/saturation zone grew to 8%, 16%, and 18% of the ice cap, respectively, as a result of the decline of the pseudo dry snow zone. Subsequently, the percolation/saturation zone declined in area from 2008 to 2011 (13%, 13%, 9% and 8%) due to the progression of the glacier ice zone to higher elevations (Figure 3.12).

The σ^0 value from 1750-1800 m along the northwest transect changed from <0 dB in 2004 and 2005 (-0.5 and -0.4 dB) to >0 dB (0.4 to 1.2 dB) from 2006 to 2011. To assess controls on the σ^0

values, they were correlated with PDDs, previous winter accumulation, and surface mass balance recorded from the mass balance stake and AWS at 1781 m (Figure 3.13). The coefficient of determination (r^2) was computed between the backscatter values and each dataset (Figure 3.13). For the correlation between PDDs and σ^0, r^2 = 0.56; between winter accumulation and σ^0, r^2= 0.52; and between surface mass balance and σ^0, r^2 = 0.31. The change in σ^0 values appear to be related to all of these factors, although only the relationship between σ^0 and PDDs is statistically significant at the 95% level (likely due to the low degrees of freedom for this relatively short dataset). The mean annual air temperature at Dev1H from 2004 to 2011 has been increasing slightly (0.05ºC a^{-1}), with main increases being seen in the summer (0.36ºC a^{-1}) and winter (0.25ºC a^{-1}) (Figure 3.9b). FDDs at Dev1H have also been increasing at a rate of 36ºC a^{-1} during this time period, reaching their highest value in 2010 of -6448ºC (Figure 3.8b).

The pseudo dry snow zone, defined as the total ice cap area above the saturation/percolation zone with a σ^0 value <0 dB, had a spatial extent of 723 km^2 in 2005 and 323 km^2 in 2006, but became nonexistent from 2007 onwards (Figure 3.12). The summit always tends to have a lower backscatter than its surroundings, indicating that the SAR signal is absorbed more in this area. This is due to the drier, lower density, and more homogeneous facies characteristics in this region, indicative of fewer internal reflectors and smaller snow crystals. Layers of different densities act as partially reflective surfaces, thus a more heterogeneous snow pack will cause backscatter (Bardel et al, 2002). For example, the ice core extracted in May 2011 at Dev3F (1731 m) showed more reflective layers (i.e. ice lenses) and density variations than a core extracted at 1781 m, which was more homogeneous (Figure 3.14). The zone of peak backscatter has been increasing in elevation since 2004, indicating that higher elevation areas are experiencing more melt.

The superimposed ice zone is seen to decrease in extent as warm summers continued to persist from 2005 to 2011. This is indicative of the ELA 'catching-up' to the EnviSat firn line as increased melt rates acted to infill pore space in the lower firn facies zones. This is seen as a consequence of the differing migration rates to higher elevation between the ELA and firn line (Figure 3.10).

It should be noted that rainfall can also occur in across the ice cap in the summer months, giving the false appearance of melt within the internal structure of the snowpack. Nonetheless, rainfall

is a rare phenomenon at high elevation on DIC, yet its impact can create a false interpretation of melt. For example, in 2006 rainfall occurred across all of DIC, which added more internal structure within the snowpack in the saturation/percolation and pseudo dry snow zones, thus causing the false appearance of higher melt in these zones (David Burgess, personal communication).

The biggest changes in the glacier facies distribution are seen in areas with gentle slopes that cover a large spatial extent. Hence, the southern portion of DIC has seen the largest progression of the glacier ice zone (Figure 3.12). The northeast portion of DIC has seen less change, likely due to its relatively steep surface. From 2004 to 2006 the dry and pseudo dry snow zone has migrated towards the summit of DIC. Likewise, from 2007 to 2011, the percolation/saturation zone has been retreating towards the summit as well.

3.6.2 Trends in surface mass balance and ELA

To put the recent changes in glacier facies in long-term context, the 2004 to 2011 mass balance record was compared with the long-term mean mass balance (1961- present) for DIC. The cumulative net balance across the northwest sector of DIC from 1961 to 2011 totaled -6307 kg m^{-2} a^{-1} (Figure 3.2). Nearly half (49%) of the total mass loss since 1963 has occurred from 2005 to 2011. Mean annual mass balance from the northwest sector during the periods 1998-2004 and 2005-2011 increased from -212 kg m^{-2} a^{-1} to -402 kg m^{-2} a^{-1}. In addition, every annual balance since 2004 has been lower than the 1981-2010 mean (-157 kg m^{-2} a^{-1}) by at least 85 kg m^{-2}.

From 1961 to 2011, the ELA in the northwest sector varied between 579 and 1570 m a.s.l. (Figure 3.15). The median ELA was located at 1199 m and the mean ELA at ~1148 m. There has been marked variability of the ELA between years (standard deviation = 243 m), with a long term increase between 1961 and 2012 at a rate of 7.7 m a^{-1} (Figure 3.15).

3.7 Discussion

From 1999 to 2005, Wolken et al (2009) used QuickScat σ^0 values and found that, on average, the glacier ice zone on DIC had been slightly decreasing in extent, indicating a lowering of the firn line boundary. However, since 2005 the EnviSat ASAR σ^0 values reported here indicate an

increase in areal extent of the glacier ice zone and an increase in the elevation of the firn line. Casey and Kelly (2010) used Radarsat-1 imagery to report an up-slope horizontal displacement of the SAR-derived firn line of ~1 km along the northwest transect from 2003 to 2006.

At lower elevations (1300 – 1600 m), the mass balance and temperature data indicate that the melt rate increased from 2004 to 2006 (Figure 3.11), which would cause the presence of more ice lenses and higher rates of firn densification. The low to high backscatter transition from 2004 to 2006 was therefore likely due to increased ice content within the firnpack below the LSS (Wang et al., 2007). Following the 2006 peak in backscatter at elevations between ~1300 and 1600 m, a gradual decrease in σ^0 was seen alongside an increase in PDDs and a physical transformation of this region of the ice cap from an accumulation area with high backscatter (firn facies), to an ablation area with low backscatter (ice facies). Engeset et al (2002) found that in negative mass balance years on Kongsvegen Glacier, Svalbard,, firn facies areas near the ELA can transform into superimposed or glacier ice zones.

The progression of the EnviSat derived firn line has major implications towards densification of DIC and mass loss due to summer runoff. The location of the runoff limit is a function of the firn line (Braithwaite et al, 1994), meaning that as the firn line increases in elevation an increased mass loss due to runoff should be expected. However, in a rapidly changing climate the ELA is migrating upwards into the previous lower accumulation area, resulting in an increase in densification as melt refreezes within the porous firn facies (Braithwaite et al., 1994). This refreezing process and creation of impermeable surface layers act to enhance runoff from the ice cap (Pfeffer et al., 1991). If the firn line is assumed to be the runoff limit, which Braithwaite et al (1994) say lie fairly close together, then ~92% of the total DIC area in 2011 lost its winter accumulation to run-off.

The rate at which the ELA (as derived from the *in situ* mass balance measurements) has been increasing on DIC since 2005 is approximately 44 m a^{-1}, whereas the rate of increase of the EnviSat firn line has been only 27 m a^{-1}. With this pattern, it can be expected that densification will increase in higher elevation areas. As a result, simple in situ mass balance stake measurements will likely underestimate the surface mass balance if internal accumulation is not accounted for.

The occurrence of little melt in the summer months and low winter temperatures were the likely causes of low backscatter values at high elevations of DIC from 2004 to 2006, enabling these regions to be classified as part of the pseudo dry snow zone. From 2006 to 2011, EnviSat ASAR σ^0 results from high elevation areas of DIC (>1700 m) show a transition from a pseudo dry snow zone to a saturation/percolation zone. *In situ* temperature data from Dev1H (1781 m) and Dev3F (1731 m) indicate that the pseudo dry snow zone on DIC from 2004 to 2006 was present due to relatively cold summer and winter temperatures. However, since the 1960s the dry snow zone has only been an intermittent phenomenon at the summit of DIC (Koerner, 2005). As summer and winter mean temperatures increased, the elimination of the pseudo dry snow zone was followed by a decrease in the saturation/percolation zone as the firn line continues to migrate to higher elevations.

SAR penetration depths into the surface can complicate the interpretation of backscatter imagery as facies zones migrate in a changing climate. The division between SAR facies zones can be offset to the true facies zone division due to the depths at which the SAR signal can penetrate into the subsurface (Bardel et al, 2002). As a result, previous summer surface layers can influence the backscatter for a given year. Therefore, it is likely that the low backscatter at high elevations was influenced by the irregular 2004 positive balance year. When putting the 2004 to 2011 changes in glacier facies zonation in context with the spike in summer temperatures and negative mass balance since 2004, it is likely that these patterns are occurring for the first time since the start of measurements on DIC in the early 1960s.

3.8 Conclusion

The glacier facies zones distinguished in ASAR imagery in this study are broader than the conventional zones described by Benson (1960). Nonetheless, since the intensity of backscatter differs considerably between firn facies and ice facies (Hall et al., 2000; Engeset et al, 2002), ASAR is useful in identifying the location of the firn line. The identification of the firn line permits two primary 'backscatter zones' (glacier/superimposed ice zone and saturation/percolation zone) to be distinguished, together with a dry snow zone at high altitudes in cold years.

The results presented here make it clear that the firn line does not follow a single elevation contour across DIC, but varies according to differing accumulation and melt rates. For example, the southeast sector of DIC experienced a smaller advance of the glacier ice zone than the northwestern sector, most likely due to the higher accumulation rates in this area. Together with ground measurements used for validation purposes, analysis of the Envisat ASAR imagery allowed for discrimination of various glacier facies zones across DIC, and assessment of the changes in area of each zone over time. By monitoring the progression of the various glacier facies zones with SAR imagery it is possible to assess the relative mass balance of large ice masses such as DIC. With anomalously high summer temperatures since 2004 (Sharp et al., 2011), the mass balance of DIC has been increasingly negative, partially due to an increase in the elevation of the firn line, which has expanded the area from which surface melt is lost from the ice cap as runoff. If the 2004 to 2011 trend in glacier facies zonation continues, DIC will become similar in form to more southerly ice caps such as the Penny and Barnes Ice Caps. At Penny Ice Cap much more melt is experienced than at DIC, resulting in a higher firn line at >1700 m (Zdanowicz et al., 2012). In the case of Barnes Ice Cap, summer melt is so intense that there is no annual firn accumulation, and accumulation only occurs through superimposed ice (Baird, 1951). In effect, these mid-arctic ice caps may be a precursor to changes that will eventually occur on DIC.

Table 3.1 Post freeze-up (autumn) EnviSat ASAR images used in this study. All images are Wide Swath mode (150m resolution) from descending orbits. Swath width: 405km. All HH polarization.

Date (mm/dd/yyyy)	Track #	Scene center [dec. deg.])	
		Latitude	Longitude
09/23/2004	341	74.75	-80.84
11/17/2005	341	75.00	-80.50
12/07/2006	341	75.39	-79.93
11/22/2007	341	75.40	-79.91
10/02/2008	341	75.00	-80.50
04/15/2010	341	74.94	-80.59
10/07/2010	341	75.01	-80.51
11/17/2011	371	75.04	-80.43

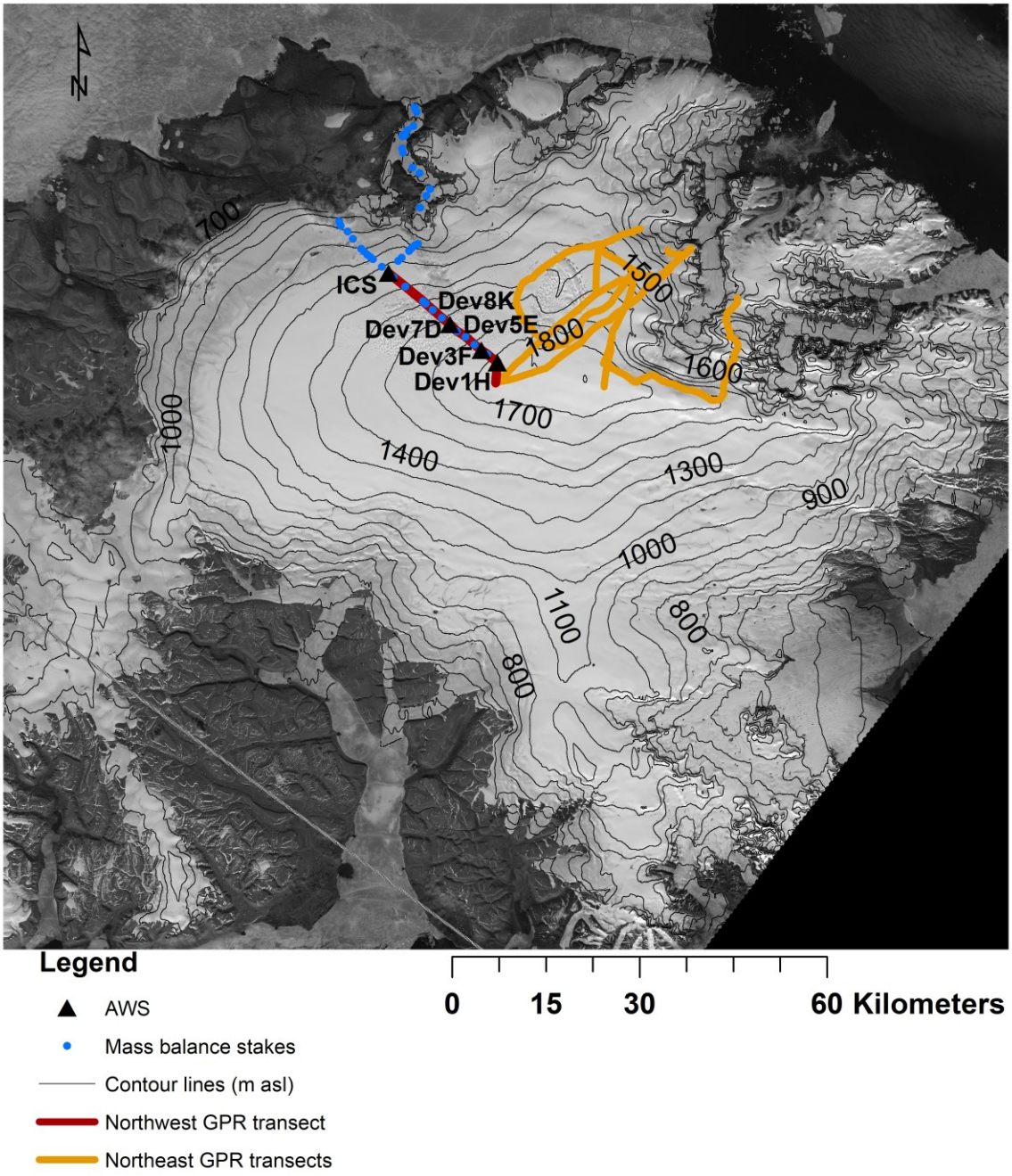

Figure 3.1. Devon Ice Cap with location of GPR transects, mass balance stakes, and AWS (Landsat 7, July 7, 2000)

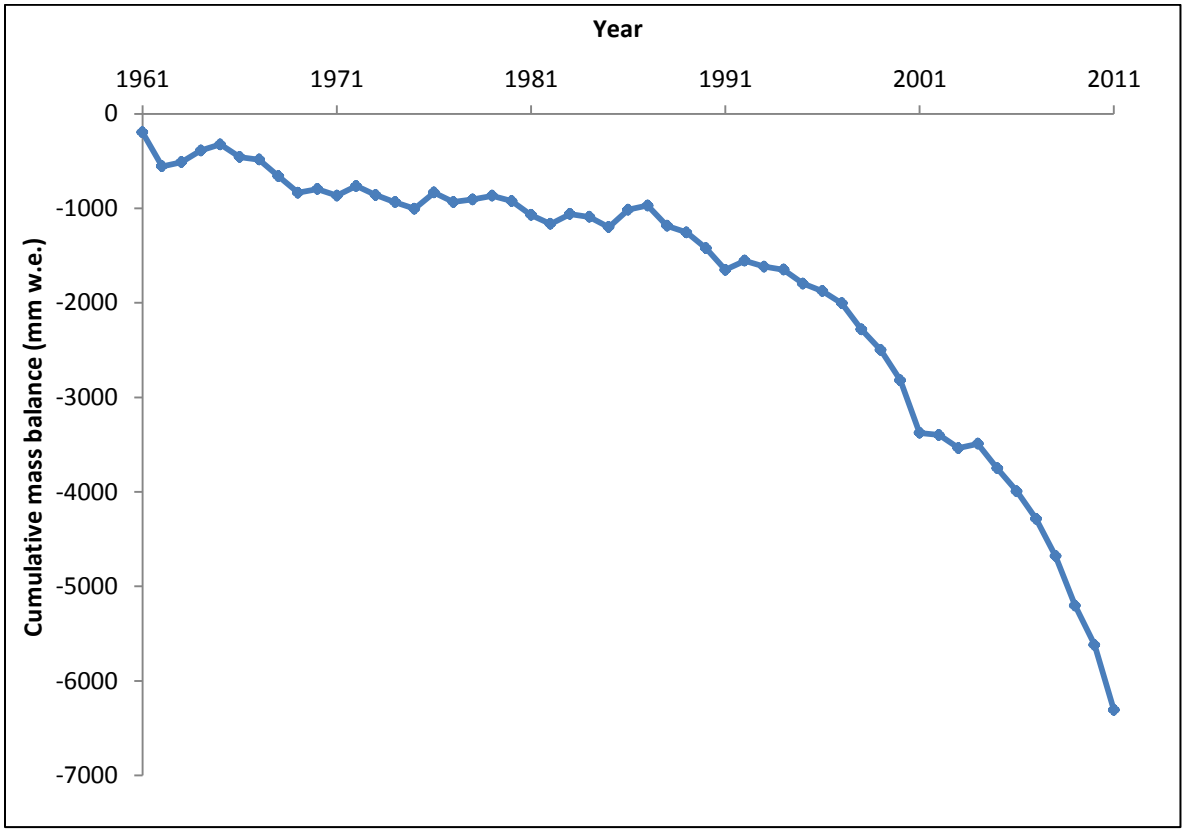

Figure 3.2. Cumulative mass balance (mm w.e.) derived from the network of mass balance stakes along the NW sector of Devon Ice Cap, 1961 - 2011

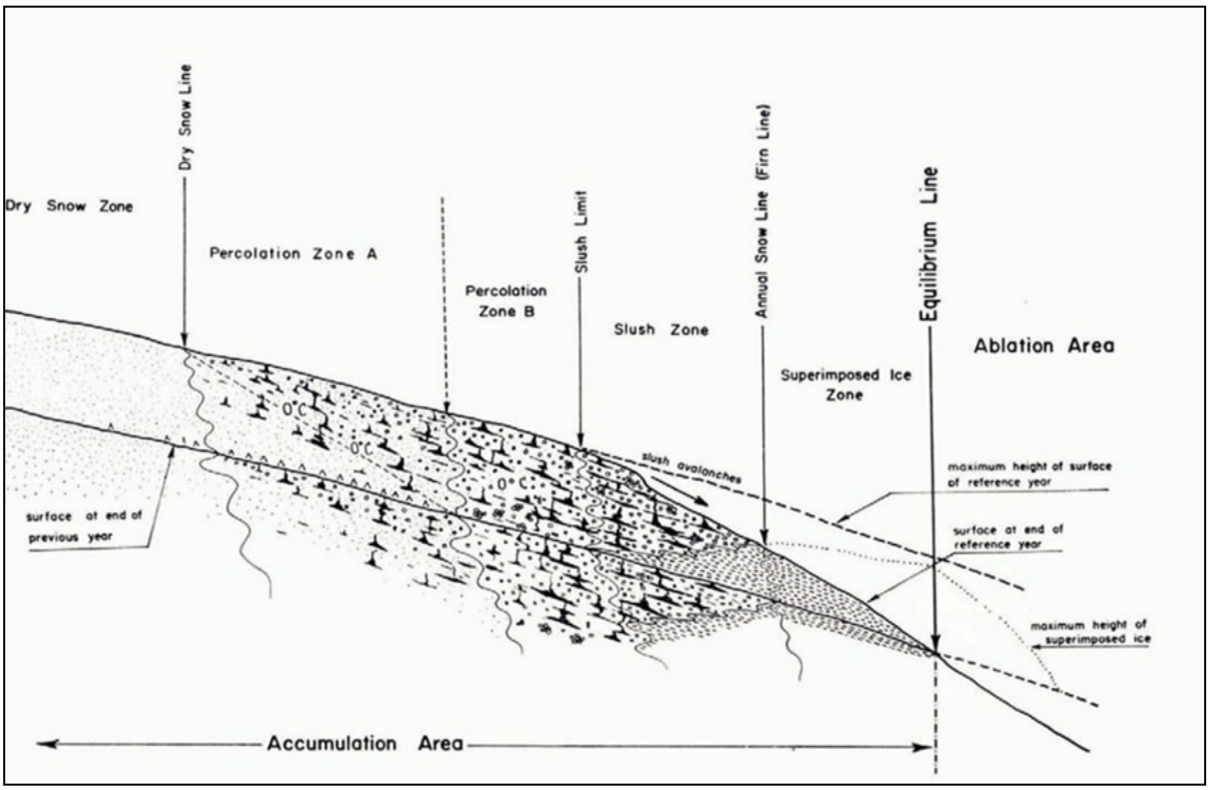

Figure 3.3. Typical glacier facies zonation on a polar ice cap as depicted by Muller (1962)

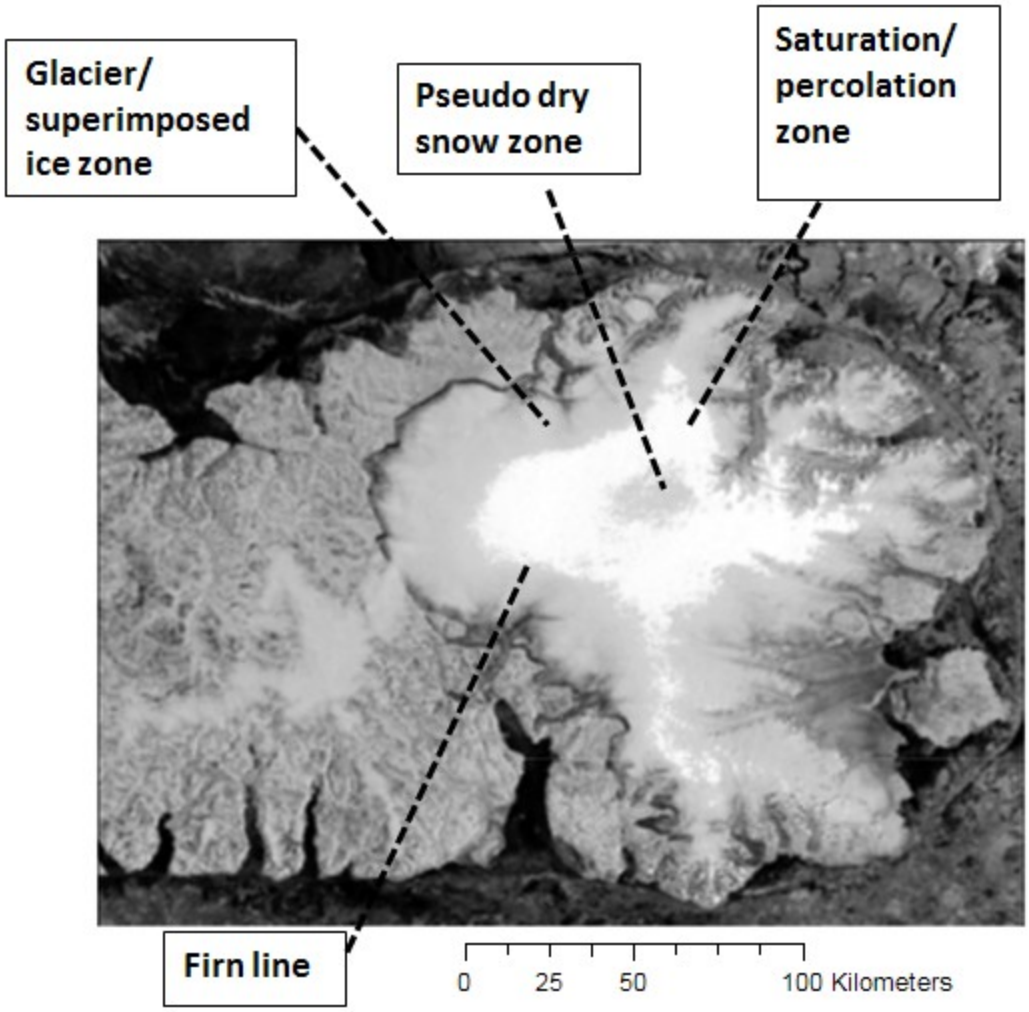

Figure 3.4. Glacier facies zones across Devon Ice Cap which are distinguishable in EnviSat ASAR imagery (Dec. 7, 2006)

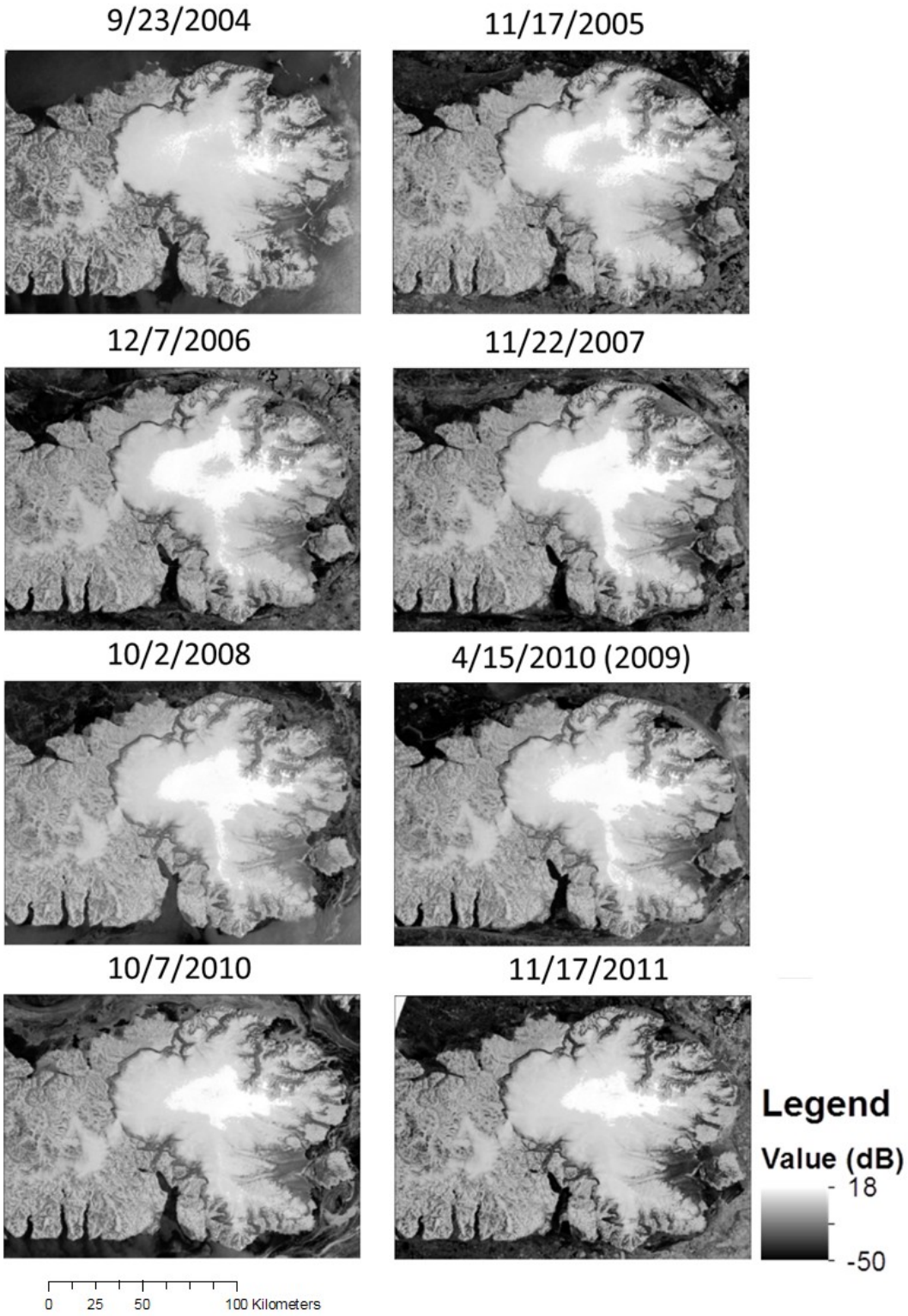

Figure 3.5. Post freeze-up EnviSat ASAR WS imagery over Devon Ice Cap from 2004 – 2011. From 2004 to 2006 high elevation areas near the summit with a lower backscatter (grey) are representative of the pseudo dry snow zone. High backscatter areas (white) depict the saturation/percolation zone. Below the saturation/ percolation zone, the low backscatter (grey and black) shows the glacier and superimposed ice zone.

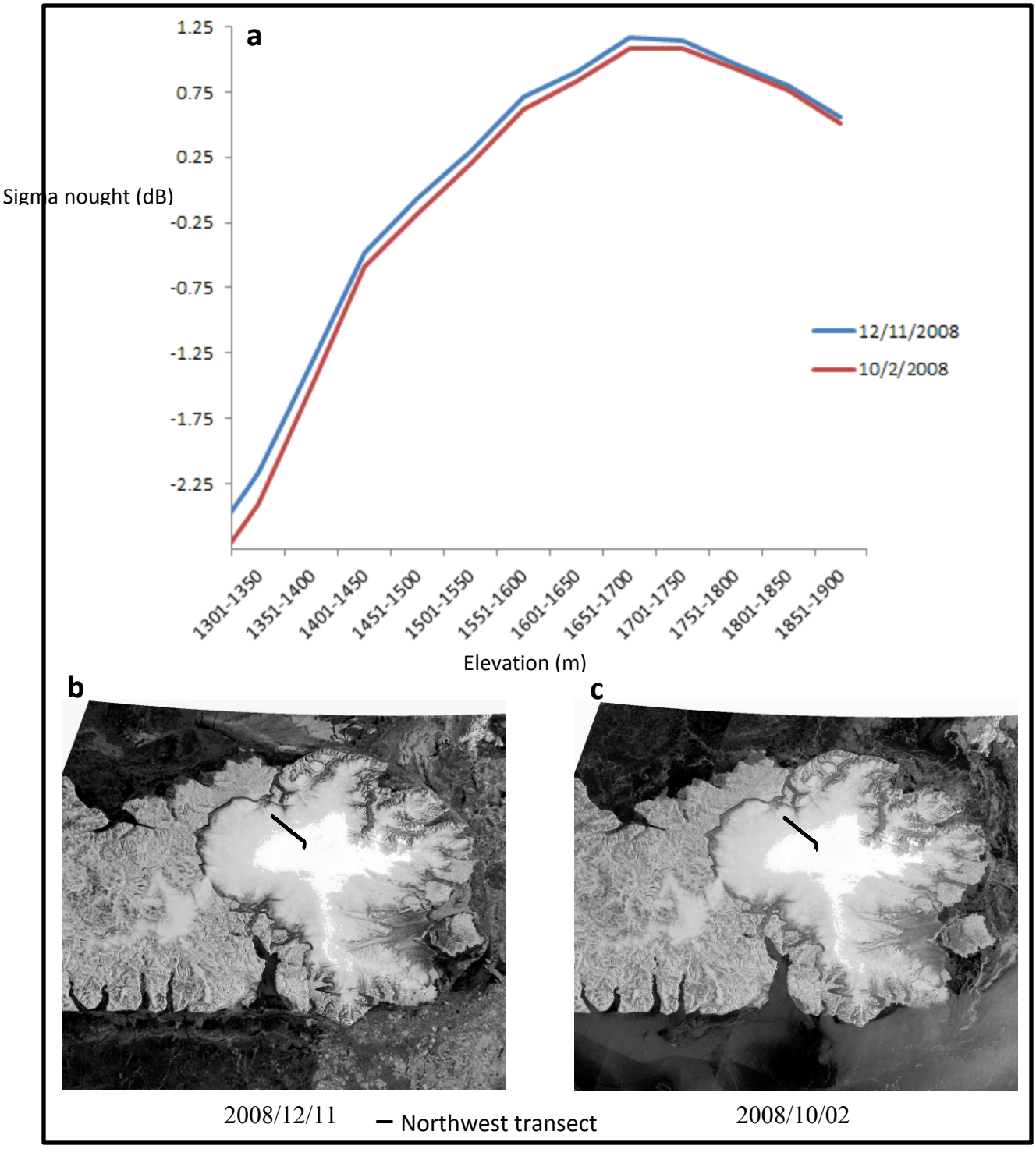

Figure 3.6 a) Extracted sigma nought along the NW transect from two EnviSat ASAR WS images acquired in the same post freeze-up year b) 2008/12/11 and c) 2008/10/02.

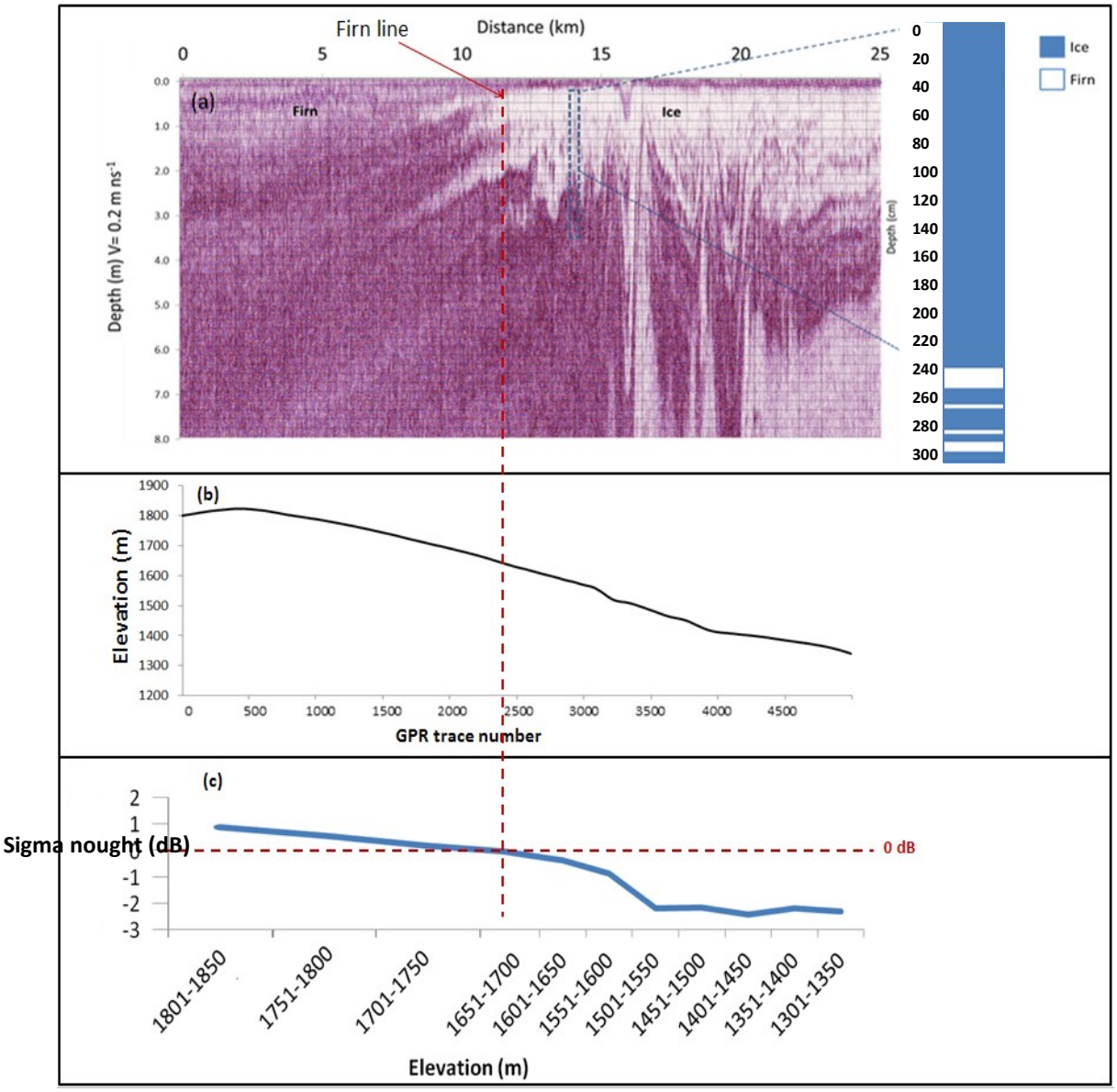

Figure 3.7. (a) May 2011 GPR radargram from the northwest transect with ice core at Dev8K (1557 m) used for validation; (b) surface elevation profile for the GPR transect; (c) extracted sigma nought from EnviSat ASAR WS image (2010/10/07) along the GPR transect. Location of GPR transect marked in Figure 3.1.

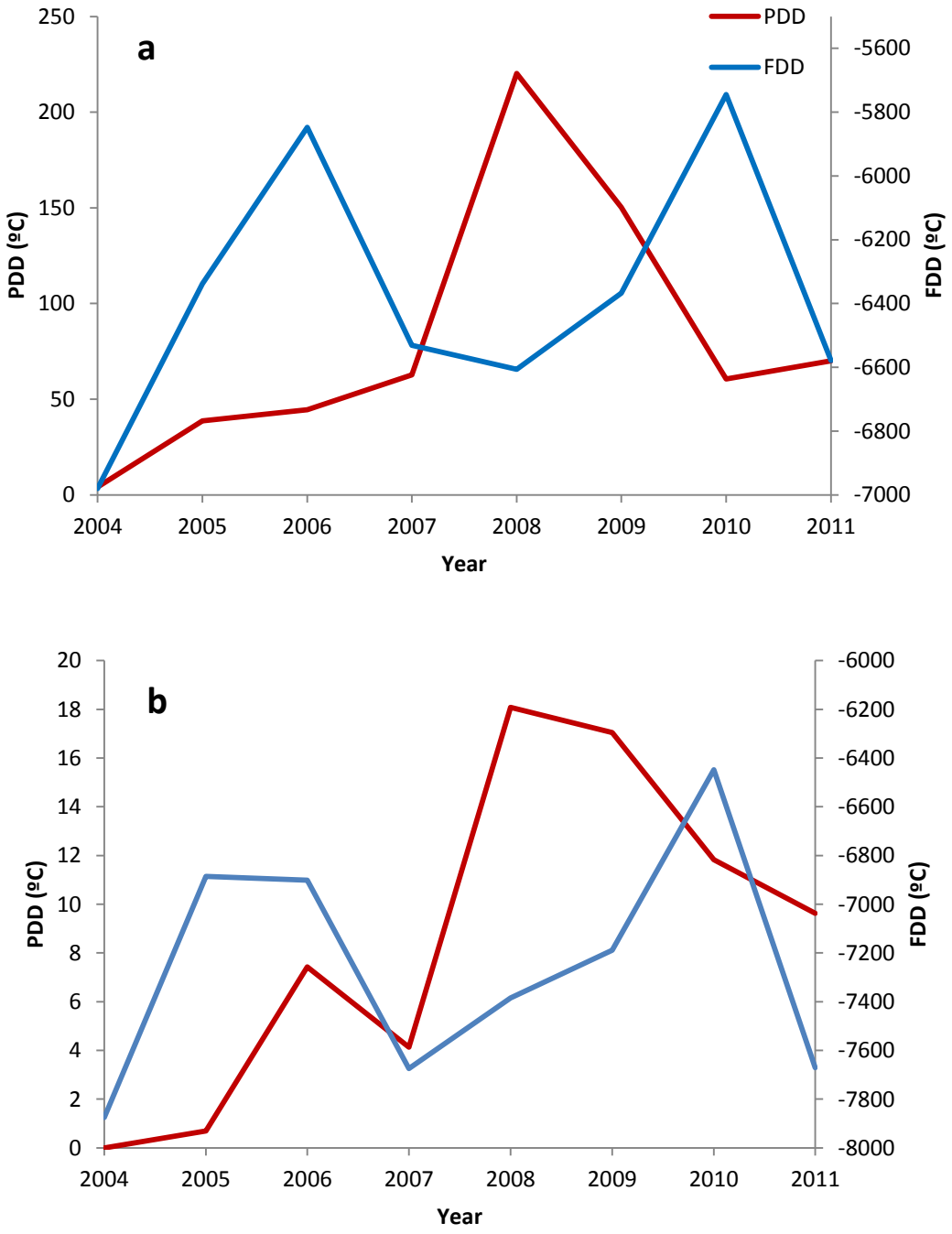

Figure 3.8. Positive and freezing degree days at (a) ICS (1317 m) and (b) Dev1H (1781 m), 2004 -2011

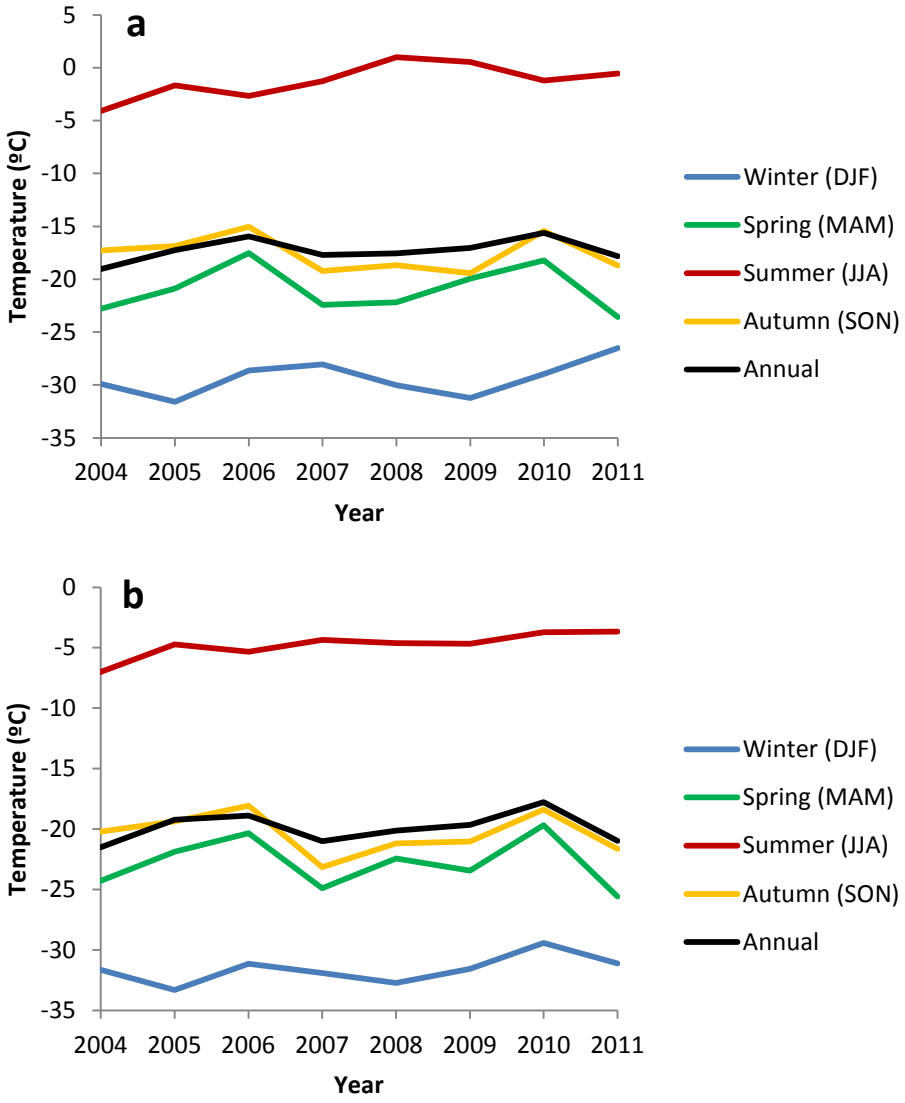

Figure 3.9. Mean seasonal temperatures from (a) ICS (1317 m) and (b) Dev1H (1781 m), 2004 – 2011

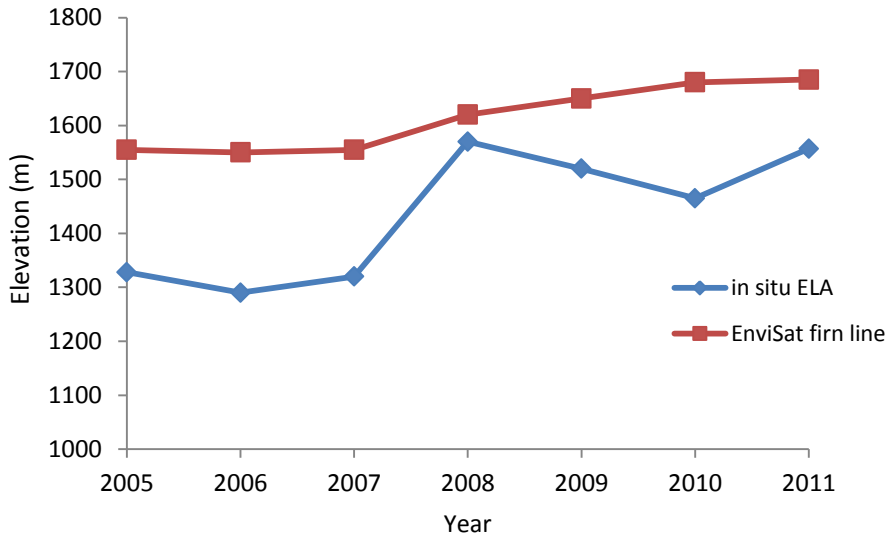

Figure 3.10. Relationship between the Envisat firn line and the in situ derived ELA, 2005-2011

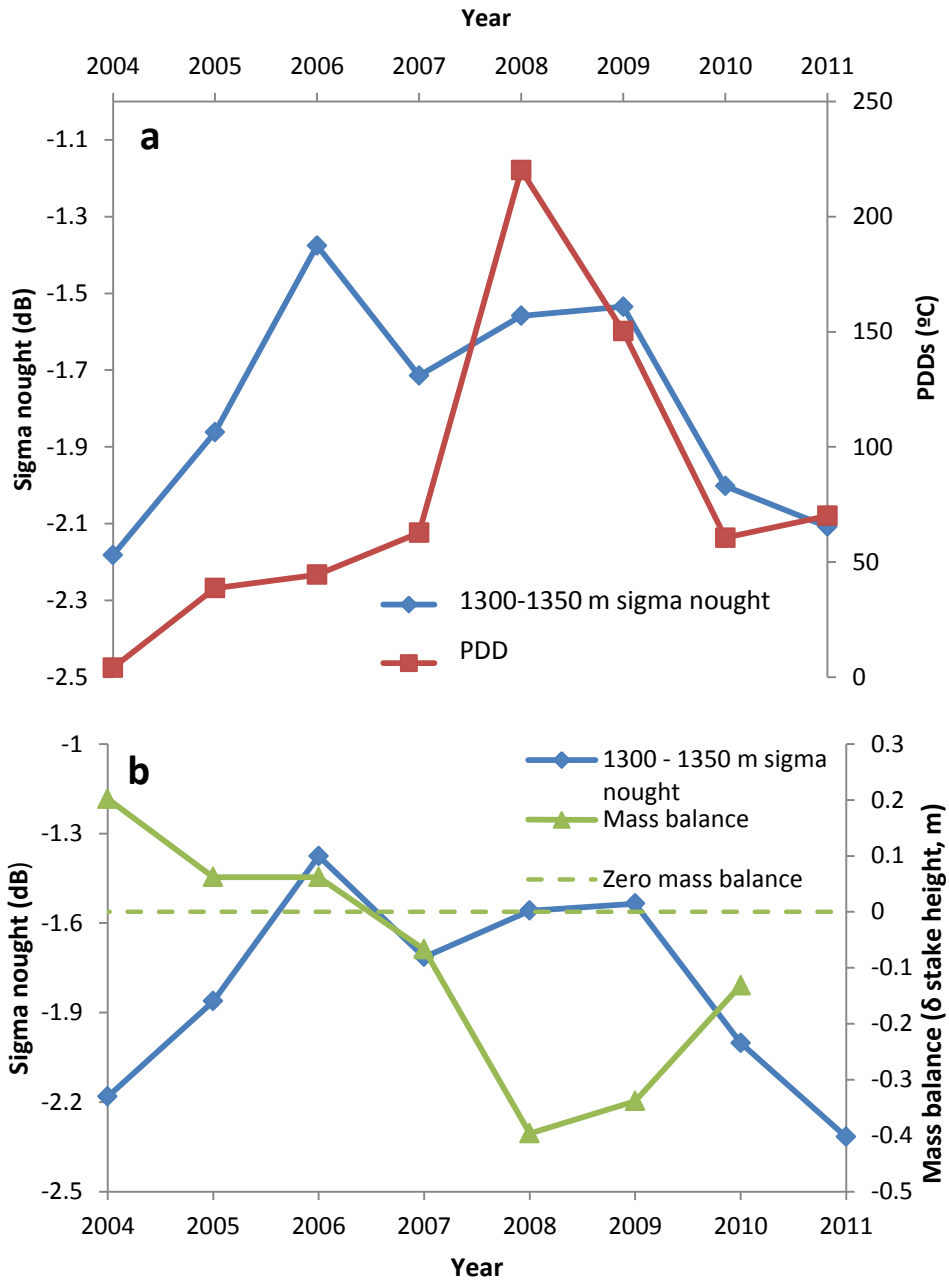

Figure 3.11. Extracted 1300-1350 m sigma nought values along NW transect in relation to (a) PDDs and (b) mass balance values at ICS (1317 m)

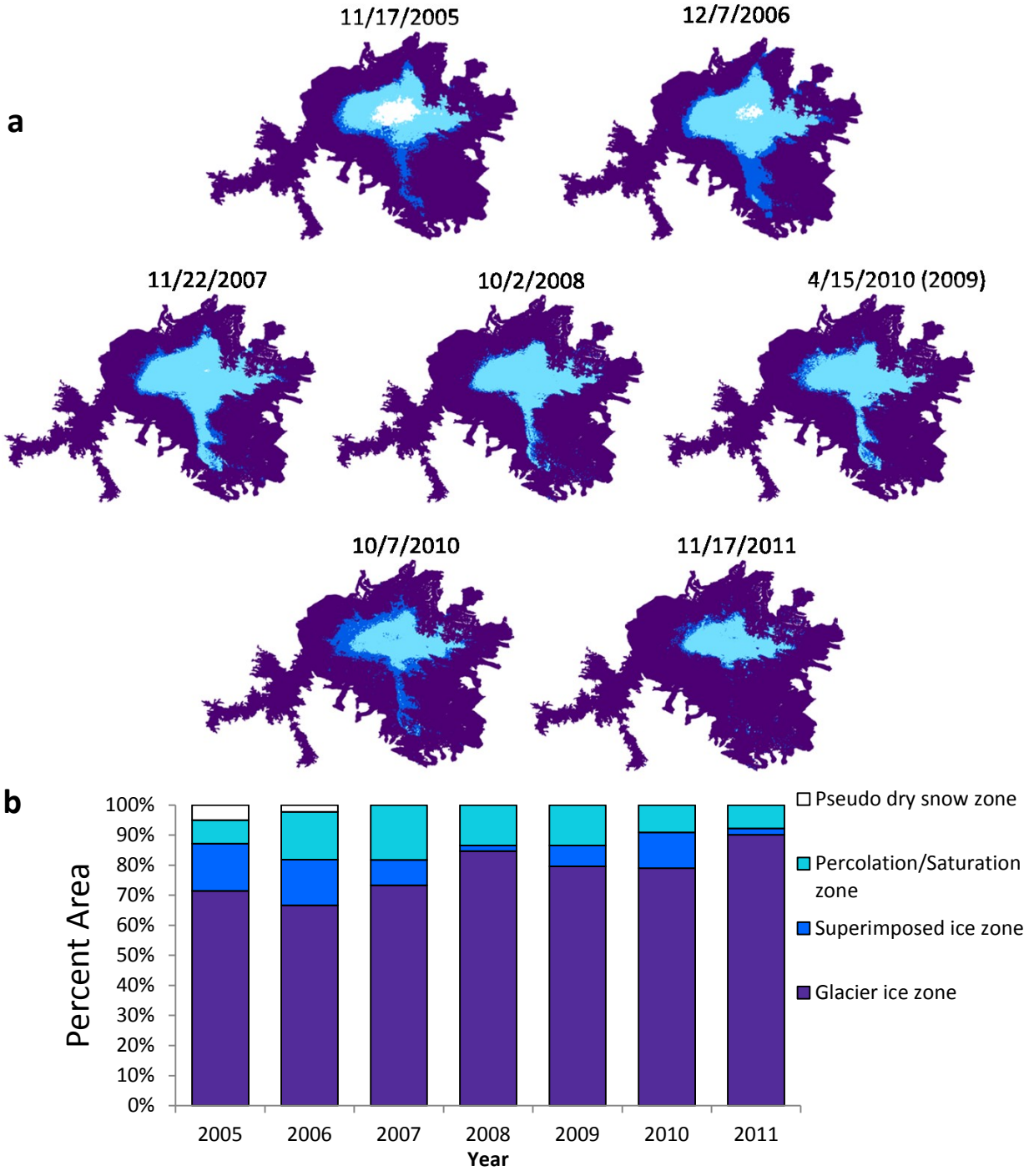

Figure 3.12. (a) Spatial extent and (b) percent area change of each facies zone based on EnviSat ASAR imagery from 2005 to 2011

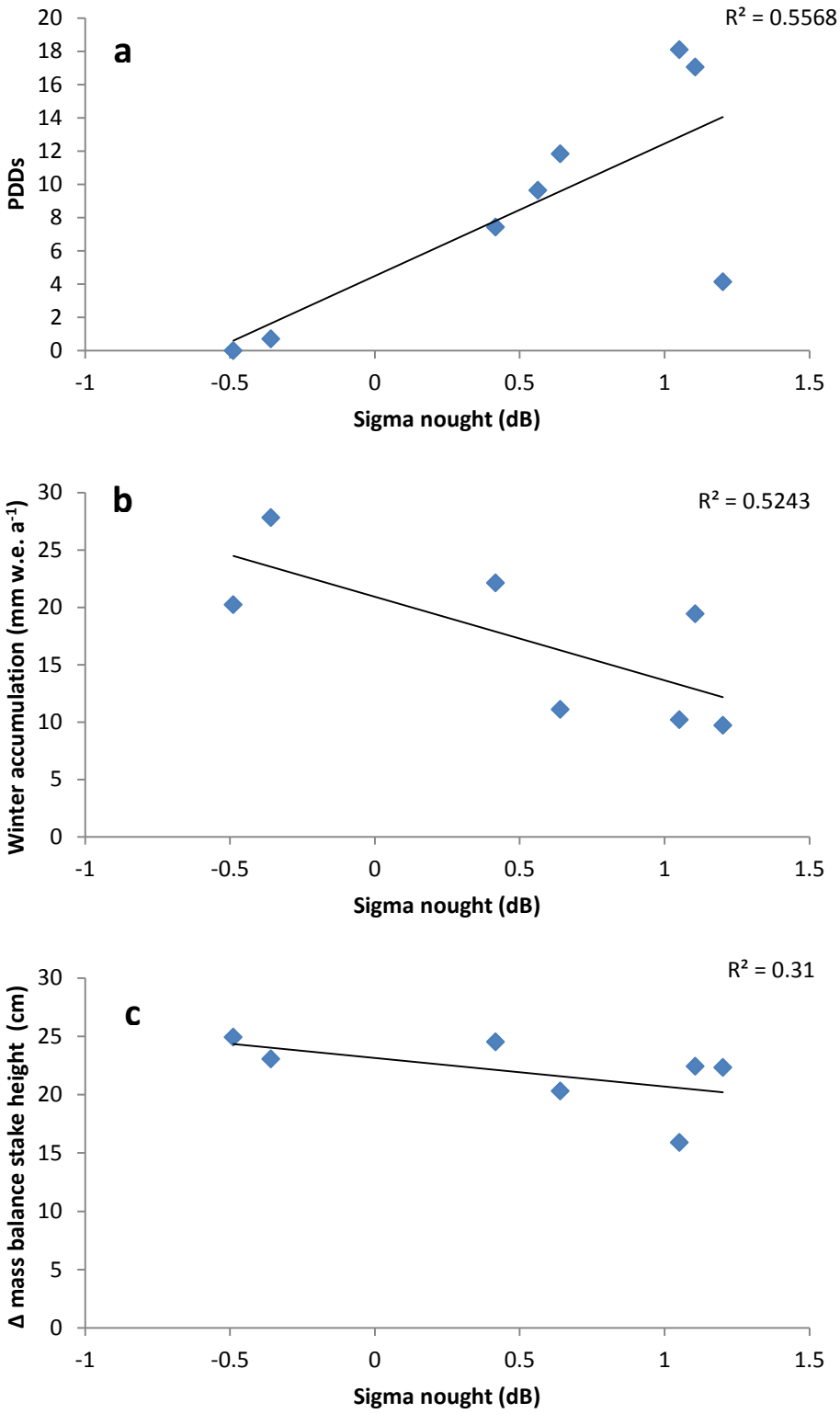

Figure 3.13. Coefficient of determination (r^2) between the extracted 1750 – 1800 m sigma nought values along the NW transect and (a) PDDs, (b) mass balance, and (c) winter accumulation at Dev1H (1781 m).

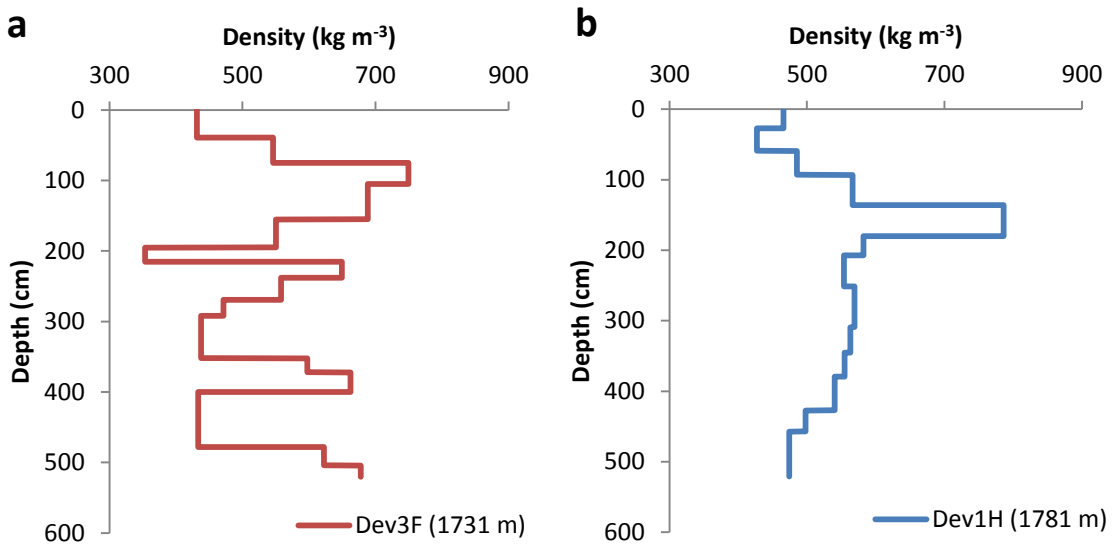

Figure 3.14. Density variability from an ice core extracted at (a) Dev3F (1731 m) and (b) Dev1H (1781 m) in May 2011

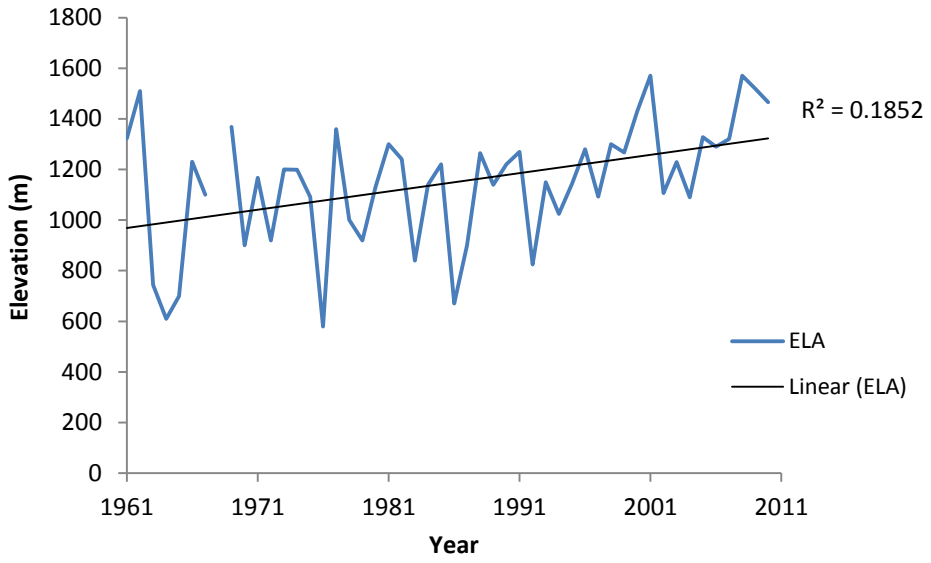

Figure 3.15. *In situ* derived ELAs from where the annual surface mass balance transitions from negative to positive net values along the northwest sector of Devon Ice Cap, 1961-2011

Chapter 4: Conclusion

The migration of facies on glaciers and ice caps is important as it has implications in terms of runoff, percolation, and densification of the near surface in the accumulation area. The spatial distribution of glacier facies zones, in particular the location of the firn line and runoff limit, will impact what happens to winter accumulation in the following summer. Below the runoff limit winter accumulation is lost to runoff in the summer, while between this limit and the dry snow zone it is refrozen internally and causes densification of the near surface. Changes in the spatial distribution of glacier facies therefore have major implications for surface and internal mass balance (Boon et al., 2010).

This study has demonstrated that EnviSat ASAR imagery can be used to monitor the annual distribution and migration of glacier facies. The 405 km width of EnviSat ASAR Wide Swath mode imagery makes it possible to assess glacier facies zonation across an entire ice cap in the Canadian Arctic at once. The glacier/superimposed ice, saturation/percolation, and pseudo dry snow zones were able to be identified in the SAR imagery, in a similar approach to other studies by Engeset et al. (2002), Langley *et al*, (2008), and Casey and Kelly (2010). Ground measurements to validate the satellite imagery from GPR transect, ice cores, near surface air temperature, and *in situ* mass balance stakes make this study unique compared to others. GPR transects from the northwest and northeast parts of Devon Ice Cap, which were used to validate the satellite imagery, are in good agreement with the ASAR results, with the position of the firn line identifiable in both. Ice cores extracted along the northwest transect were used to validate and distinguish firn and ice facies in the radargrams. Overall, the ground validation measurements of the ASAR imagery provide good support for this technique to be interpolated ice cap wide.

Data from Wolken et al (2009) using QuickScat, a spaceborne radar scatterometer, suggested that the mean firn line from glaciers and ice caps in the CAA slightly decreased in elevation from 1999 to 2005. In contrast, this study has shown an increase in elevation of the firn line, associated with the elimination of a pseudo dry snow zone and an upslope migration of the glacier and superimposed ice zones over DIC from 2004 to 2011. This is in agreement with Casey and Kelly (2010), who reported an up-slope migration of the firn line in the northwest sector of DIC of ~1 km from 2003 to 2006. From 2006 to 2011, the up-slope migration of the firn line has progressed another ~6 km in the northwest sector.

In 2011, 92% of the total area of DIC was below the firn line, compared to 87% in 2005. This change in the spatial distribution of glacier facies was found to be related to an increase of 0.36 ºC a^{-1} in summer temperatures, and 0.25ºC a^{-1} in winter temperatures, at Ice Cap Station (1317 m) since 2004. Mass balance rates from the northwest transect from 2005 to 2011 (−402.4 mm w.e. a^{-1}) are nearly twice as negative as the 1998 to 2004 rates (−212.2 mm w.e. a^{-1}), which coincides with the increase in glacier/superimposed ice zone since 2005. This 2005 to 2011 mass balance rate equates to 5.9 Gt a^{-1} when multiplied over the entire ice cap area (14 400 km^2). The 2003 to 2010 mass balance rates equate to 4 Gt a^{-1}, meaning that DIC contributed approximately 12% of the total mass loss from the CAA during this period when compared the Jacob et al. (2012) results.

Since the elimination of the pseudo dry snow zone on DIC in 2007, and the upslope migration of the firn line, it is likely that the near surface in the accumulation area has experienced considerable densification as high elevation areas have experienced higher melt rates. Ice core records from DIC show an increase in melt features and consequent densification at high elevations since the mid-1990s (Fisher et al., 2011; Colgan and Sharp 2008). At the same time,

the firn line and runoff limit have also been migrating upslope, which has caused an increase in the surface area vulnerable to mass loss due to meltwater runoff.

Across the CAA, an increase in summer temperatures (relative to the 2000-2004 mean) of between 0.8 and 2.2ºC since 2005 has been documented at various weather stations across the archipelago (Sharp et al., 2011). Zdanowicz et al. (2012) have reported a rapid warming of firn at a depth of 10 m in the accumulation area of Penny Ice Cap, Baffin Island, from ~-13ºC in 2000 to ~-3ºC in 2011. This warming across the Canadian Arctic suggests that the progression of glacier facies to higher elevations is likely being experienced on other glaciers and ice cap in the CAA.

This also implies that a densification in the near surface of accumulation areas is likely to be occurring across this region, along with an increase in the mean firn line and runoff limit, thus increasing the mass loss due to runoff. In Greenland, throughout the lower percolation zone, densification of the near-surface has been observed through ICESat's laser altimeter from 2003 to 2008, and has resulted in a surface lowering of up to 0.8 m a^{-1} in the southeast sector of the ice sheet (Bolch et al., 2013).

In conclusion, changes in glacier facies zonation that impact surface runoff, internal accumulation, and hence the surface mass balance of DIC are important to assess its contribution to future sea level rise. According to the IPCC (2007), climate change will affect small glaciers and ice caps such as DIC at a much quicker rate than the large ice-sheets. DIC may therefore serve as a useful proxy for future large scale changes to the Greenland and Antarctic ice sheets.

References

Abdalati, W., Krabill, W., Frederick, E., Manizade, S., Martin, C., Sonntag, J., Swift, R., Thomas, R., Yungel, J., and Koerner, R. (2004). Elevation changes of ice caps in the Canadian Artic Archipelago. *Journal of Geophysical Research.* **109** (F04007).

Baird, P., Ward, W. and Orvig, S. (1951). The Glaciological Studies of the Baffin Island Expedition, 1950. *Journal of Glaciology*. **2** (11), 2-9.

Bardel, P., Fountain, A., Hall, D. and Kwok, R. (2002). Synthetic aperture radar detection of the snowline on Commonwealth and Howard Glaciers, Taylor Valley, Antarctica. *Annals of Glaciology*. **34**, 177-183.

Benson, C. (1960). Stratigraphic studies in the snow and firn of the Greenland ice sheet. *Dissertation (Ph.D.)* California Institute of Technology

Binder, D., Bruckl, E., Roch, K., Behm, M., Schoner, W. and Hynek, B. (2009). Determination of total ice volume and ice-thickness distribution of two glaciers in the Hohe Tauern, Eastern Alps, from GPR data. *Annals of Glaciology.* **50**(51), 71-79.et

Bolch, T., Sandberg Sorensen, L., Simonsen, S., Molg, N., Machguth, H., Rastner., P., and Paul, F. (2013). Mass loss of Greenland's glacier and ice caps 2003-2008 revealed from ICESat laser altimetry data. *Geophysical Research Letters*. **40**, 875-881.

Boon, S., Burgess, D., Koerner, R., and Sharp, M. (2010). Forty-seven years of Research on the Devon Island Ice Cap, Arctic, Canada. *Arctic*, **63** (1), 13-29

Born M., and Wolf, E. (1999) Electromagnetic theory of propagation, interference and diffraction of light. *Cambridge University Press*. 7ed.

Braithwaite, R., Laternser, M., and Pfeffer, T. (1994). Variations of near-surface firn density in the lower accumulation area of the Greenland ice sheet, Pikitsoq, West Greenland. *Journal of Glaciology,* **40** (136), 477-485.

Brown, I. (2012). Synthetic Aperture Radar Measurements of a retreating Firn Line on a Temperate Icecap. *IEEE Journal of selected Topics in Applied Earth Observations and Remote Sensing*. **5**(1) 153-160.

Burgess, D. and Sharp, M. (2004). Recent Changes in Areal Extent of the Devon Ice Cap, Nunavut, Canada. *Arctic, Antarctic, and Alpine Research,* **36(**2), 261-271.

Canada Centre for Remote Sensing (2007). Fundamentals of Remote Sensing. Natural Resources Canada, Ottawa. ON. Available from http://www.nrcan.gc.ca/earth-sciences/geography-boundary/remote-sensing/fundamentals/1430 [cited April 2, 2013].

Canadian Space Agency (2011). Satellite Characteristics. *Government of Canada*. Available from http://www.asc-csa.gc.ca/eng/satellites/radarsat/radarsat-tableau.asp [Cited April 2, 2013]

Casey, JA. and Kelly, R. (2010). Estimating the equilibrium line of Devon Ice Cap, Nunavut, from RADARSAT-1 ScanSAR wide imagery. *Canadian Journal of Remote Sensing*, **36** (1) S41-S55.

Cavalieri, D. and Parkinson, C. (2012). Arctic sea ice variability and trends, 1979-2010. *The Cryosphere*. **6**(4), 881-889.

Clausen, H. B., N. S. Gundestrup, S. J. Johnsen, R. Bindschadler, and J. Zwally (1988), Glaciological investigations in the Crete area, central Greenland: A search for a new deep-drilling site, *Annals of Glaciology*, 10, 10–15.

Colgan, W. and Sharp, M. (2008). Combined oceanic and atmospheric influences on net accumulation on Devon Ice Cap, Nunavut, Canada. *Journal of Glaciology,* **54** (184) 28-40.

Conway, H., Smith, B., Vaswani, P., Matsuoka, K., Rignot, E. and Claus, P. (2009). A low-frequency ice-penetrating radar system adapted for use from an airplane: test results from Bering and Malaspina Glaciers, Alaska, USA. *Annals of Glaciology*. **50** (51), 93-97.

Copland, L., Mueller, D. and Weir, L. (2007). Rapid loss of the Ayles Ice Shelf, Ellesmere Island, Canada. *Geophysical Research Letters*. **34**, L21501.

Daida, J., Onstott, R., Bersano-Begey, T., Ross, S. and Vesecky, J. (1996). Ice roughness classification and ERS SAR imagery of Arctic sea ice: evaluation of feature-extraction algorithms by genetic programming. *International Geoscience and Remote Sensing Symposium, 1996. IGARSS '96. 'Remote Sensing for a Sustainable Future.'* **3**, 1520-1522.

Dall, J. (2007). InSAR elevation bias caused by penetration into uniform volumes. *Geoscience and Remote Sensing, IEEE Transactions on*, **45**(7), 2319–2324.

Davies, C. and Poznyak V. (1993). The depth of penetration in Antarctic firn at 10 GHz. *IEEE Transactions in Geoscience Remote Sensing.* **31**(5). 1107-1111.

Dowdeswell, J.A., T.J. Benham, M.R. Gorman, D. Burgess and M. Sharp. (2004). Form and flow of the Devon Island ice cap, Canadian Arctic. *Journal of Geophysical Research,* **109**, 1-14.

Drinkwater, M. and Long, D. (1998). Seasat, ERS-1/2 and NSCAT scatterometer observed changes on the large ice sheets. *Geoscience and Remote Sensing Symposium Proceedings*. **4**, 2252-2254

Dyurgerov, M. and Meier, M. (2005). Glaciers and the changing earth system: A 2004 snapshot. *Institute of Arctic and Alpine Research: University of Colorado Boulder*. Occasional Paper, **58**

Elachi, C. (1987). Introduction to the Physics and Techniques of Remote Sensing. J. A. Kong ed*., John Wiley and Sons*, 413 pp

Engeset, R., Kohler, J., Melvold, K., and Lunden, B. (2002). Change detection and monitoring of glacier mass balance and facies using ERS SAR winter images over Svalbard. *International Journal of Remote Sensing*. **23** (10). 2023-2050.

European Space Agency (2013). ESA Earth Observation Missions. *Earth Observation Ground Segment Department*. Available from https://earth.esa.int/web/guest/missions/esa-operational-eo-missions/ [cited April 2, 2013]

Fisher, D., Zheng, J., Burgess, D., Zdanowicz, C., Kinnard, C., Sharp, M. and Bourgeois, J. (2011). Recent melt rates of Canadian arctic ice caps are the highest in four millennia. *Global and Planetary Change*, 1-5.

Forster, R., Isacks, B. and Das, S. (1996). Shuttle imaging radar (SIR-C/X-SAR) reveals near-surface properties of the South Patagonian Icefield. *Journal of Geophysical Research*. **101** E10, 23,169-23,180.

Forster, R., Jezek, K., Bolzan, J., Baumgartner, F. and Gogineni, S. (1999). Relationships between radar backscatter and accumulation on the Greenland ice sheet.*International Journal of Remote Sensing*. **20**(15-16) 3131-3147.

Gardner, A., Moholdt G., Wouters, B., Wolken, G., Burgess, D., Sharp, M., Cogley, G., Braun, C. and Labine, C. (2011). Sharply increased mass loss from glaciers and ice caps in the Canadian Arctic Archipelago. *Nature*, **473** (7347), 357-360.

Glen, J. and Paren, J. (1975). The electrical properties of snow and ice. *Journal of Glaciology*, **15**(73), 15-38.

Hall, D., Williams Jr., S., Barton, J., Sigurdsson, O., Smith, L. and Garvin, J. (2000). Evaluation of remote-sensing techniques to measure decadal-scale changes of Hofsjokull ice cap, Icaland. *Journal of Glaciology*. **46**(154), 375-388.

Jacob, T., Wahr, J., Pfeffer, T. and Swenson, S. (2012). Recent contributions of glaciers and ice caps to sea level rise. *Nature*. **482**, 514-518.

Johnsen, H., Lauknes, L. and Guneriussen, T. (1995). Geocoding of fast-delivery ERS-1 SAR image mode product using DEM data. *International Journal of Remote Sensing*. **16**(11), 1957-1968.

Koerner, R. (1966). Accumulation on the Devon Island ice cap, Northwest Territories, Canada. *Journal of Glaciology,* **6 (**45), 383-393.

Koerner, R. (1970). The mass balance of the Devon Island Ice Cap, Northwest Territories, Canada, 1961-1966. *Journal of Glaciology*, **9**(57), 325-226.

Koerner, R. (2005). Mass balance of glaciers in the Queen Elizabeth Islands, Nunavut, Canada. *Annals of Glaciology,* **42,** 417-423.

Konig, M., Wadham, J., Winther, J.G., Kohler, J. and Nuttall, A.M. (2002). Detection of superimposed ice on the glaciers Kongvegen and midre Lovénbreen, Svalbard, using SAR satellite imagery. *Annals of Glaciology*. **34**. 335-342.

Kovacs, A., Gow, A.J. and Morey, R.M., 1995. The in-situ dielectric constant of polar firn revisited. *Cold Regions Science and Technology*, **23**(3), 245-256.

Langley, K., Hamran, S.E., Hogda, K.A., Storvold, R., Brandt, O., Kohler, J. and Hagen, JO (2008). From Glacier Facies to SAR Backscatter Zones via GPR. *IEEE Transactions on Geoscience and Remote Sensing*, **46** (9), 2506-2515.

Lenaerts, J., van Angelen, J., van den Broeke, M., Gardner, A., Wouters, B. and van Meijgaard, E. (2013). Irreversible mass loss of Canadian Arctic Archipelago glacier. *Geophysical Research Letters*. Accepted Article.

Lillesand, T., Kiefer, R. and Chipman, J. (2008). Remote sensing and image interpretation. *John Wiley and sons*. 6 ed.

Mair, D., Burgess, D. and Sharp M. (2005). Thirty-seven year mass balance of Devon Ice Cap, Nunavut, Canada determined by shallow ice coring and melt modeling. *Journal of Geophysical Research*, **110**, 1-13.

Marshall, G., Rees, W. and Dowdeswell, J. (1995). The discrimination of ERS-1 SAR data. *Sensors and Environmental Applications of Remote Sensing*. 263-269.

Massom, R. and Lubin, D. (2006). Polar remote sensing, *Springer-Verlag*. 2ed.

Matzler, C. and Wegmuller, U. (1987). Dielectric properties of fresh-water ice at microwave frequencies. *Journal of Applied Physics*. **20**, 1623-1630.

Meese, D., A. J. Gow, P. Grootes, P. A. Mayewski, M. Ram, M. Stuiver, K. C. Taylor, E. D. Waddington, and G. A. Zielinski (1994). The accumulation record from the GISP2 core as an indicator of climate change throughout the Holocene, *Science*, 266, 1680–1682

Moorman, B. and Michel, F. (2000). Glacial hydrological system characterization using ground-penetrating radar. *Hydrological Processes*. **14**. 2645-2667.

Muller, F. (1962). Zonation in the accumulation area of the glaciers of Axel Heiberg Island, N.W.T., Canada. *Journal of Glaciology*, **4** (33), 302-311.

National Snow and Ice Data Center (2012). Artic sea ice extent settles at record seasonal minimum. *University of Colorado Boulder*. Available from http://nsidc.org/arcticseaicenews/2012/09/arctic-sea-ice-extent-settles-at-record-seasonal-minimum/ [Cited April 2, 2013].

Nghiem, S., Hall, D., Mote, T., Tedesco, M., Albert, M., Keegan, K., Shuman, C., DiGirolamo, N. and Neumann, G. (2012). The extreme melt across the Greenland ice sheet in 2012. *Geophysical Research Letters*. **39**, L20502.

Nolan, A., Fetterer, F., and Scambos, T. (2002). Surface roughness characterizations of sea ice and ice sheets: case studies with MISR. *IEEE Transactions on Geoscience and Remote Sensing*. **40**(7), 1605-1615.

Onstott, R. (1992). Microwave Remote Sensing of Sea Ice. Frank D. Carsey ed*., Geophysical monograph*, 73-104.

Palli, A., Kohler, J., Isaksson, E., Moore, J., Pinglot, J.F., Pohjola, V. and Samuelsson, H. (2002). Spatial and temporal variability of snow accumulation using ground-penetrating radar and ice cores on a Svalbard glacier. *Journal of Glaciology*. **48** (162) 417-424.

Partington, KC. (1998). Discrimmination of glacier facies using multi-temporal SAR data. *Journal of Glaciology*, **44** (146), 42-53.

Pfeffer, T., Meier, M., and Illangasekare, T. (1991). Retention of Greenland Runoff by Refreezing: Implications for Projected Future Sea Level Change. *Journal of Geophysical Research*, **96** (C12). 117-22.

Quincey, DJ. And Luckman, A. (2009). Progress in satellite remote sensing of ice sheets. *Progress in Physical Geography*, **33** (4), 547-567.

Radic, V. and Hock, R. (2010). Regional and global volumes of glaciers derived from statistical upscaling of glacier inventory data. *Journal of Geophysical Research*. **115**(F1).

Rignot, E., Echelmeyer, K. and Krabill, W. (2001). Penetration depth of interferometric synthetic-aperture radar signals in snow and ice. *Geophysical Research Letters*. **28** (18), 3501-3504.

Rignot, E., and Kanagaratnam, P. (2006). Changes in the velocity structure of the Greenland ice sheet. *Science*, **311**,. 986-990.

Sharp, M., Burgess, D., Cogley, G., Ecclestone, M., Labine, C. and Wolken, G. (2011) Extreme melt on Canada's Arctic ice caps in the 21st century. *Geophysical Research Letters,* **38**, 1- 5.

Schoof, C. (2010). Ice-sheet acceleration driven by melt supply variability. *Nature*, **468**, 803-806.

Sundal, A. V., Shepherd, A., Nienow, P., Hanna, E., Palmer, S. and Huybrechts, P. (2011). Melt-induced speed-up of Greenland ice sheet offset by efficient subglacial drainage. *Nature*. **469**, 521-524.

Sylvestre, T. Spatial Patterns of Snow Accumulation across the Belcher Glacier Basin, Devon Island, Nunavut, Canada Devon Island, Nunavut, Canada. (2009). Master's Thesis. University of Ottawa.

Tiuri, M., Sihvola, A., Nyfors, E. and Hallikaiken, M. (1984). The complex dielectric constant of snow at microwave frequencies. *IEEE Journal of Oceanic Engineering*. **9** (5), 377 – 382.

Ulaby, F., Moore, R. and Fung, A. (1986). Microwave remote sensing, active and passive. Reading, MA. *Addison-Wesley Publishing Co*. 3ed.

van de Wal, RS., Boot, W., Van den Broeke, M.R., Smeets, C.J.P.P, Reijmer, C.H, Donker, J.J.A. and Oerlemans. J. (2008). Large and rapid Melt-Induced velocity changes in the ablation zone of the Greenland Ice Sheet. *Science*, **321,** 111-113.

Van Wychen, W., Copland, L., Gray, L., Burgess, D., Danielson, B. and Sharp, M. (2012). Spatial and temporal variation of ice motion and ice flux from Devon Ice Cap, Nunavut, Canada. *Journal of Glaciology*. **58**(210), 657-664.

Wang, L., Sharp, M., Rivard, B. and Steffen, K. (2007). Melt season duration and ice layer formation on the Greenland ice sheet, 2000 – 2004. *Journal of Geophysical Research*. **112** (F4).

Wolken, GJ., Sharp, M. and Wang, L. (2009). Snow and ice facies variability and ice layer formation on Canadian Arctic ice caps, 1999-2005. *Journal of Geophysical Research*, **114**, 1-14.

Zahnen, N., Jung-Rothenhäusler, F., Oerter, H., Wilhelms, F. and Miller, H. (2002). Correlation between Antarctic dry snow properties and backscattering characteristics in RADARSAT SAR imagery. *EARSeL eProceedings* **2**, 140–148.

Zdanowicz, C., Smetny-Sowa, A., Fisher, D., Schaffer, N., Copland, L., Eley, J. and Dupont, F. (2012). Summer melt rates on Penny Ice Cap, Baffin Island: Past and recent trends and implications for regional climate. *Journal of Geophysical Research*, **117** (F2), 1-21.

Zhang, J., Lindsay, R., Schweiger, A. and Steele, M. (2013). The impact of an intense summer cyclone on 2012 Arctic sea ice retreat. *Geophysical Research Letters.* **40**.

Zwally, H.J., Abdalati, W., Herring, T., Larson, K., Saba, J. and Steffen, K. (2002). Surface Melt-Induced Acceleration of Greenland Ice-Sheet Flow. *Science,* **297**, 218-222.

Appendix

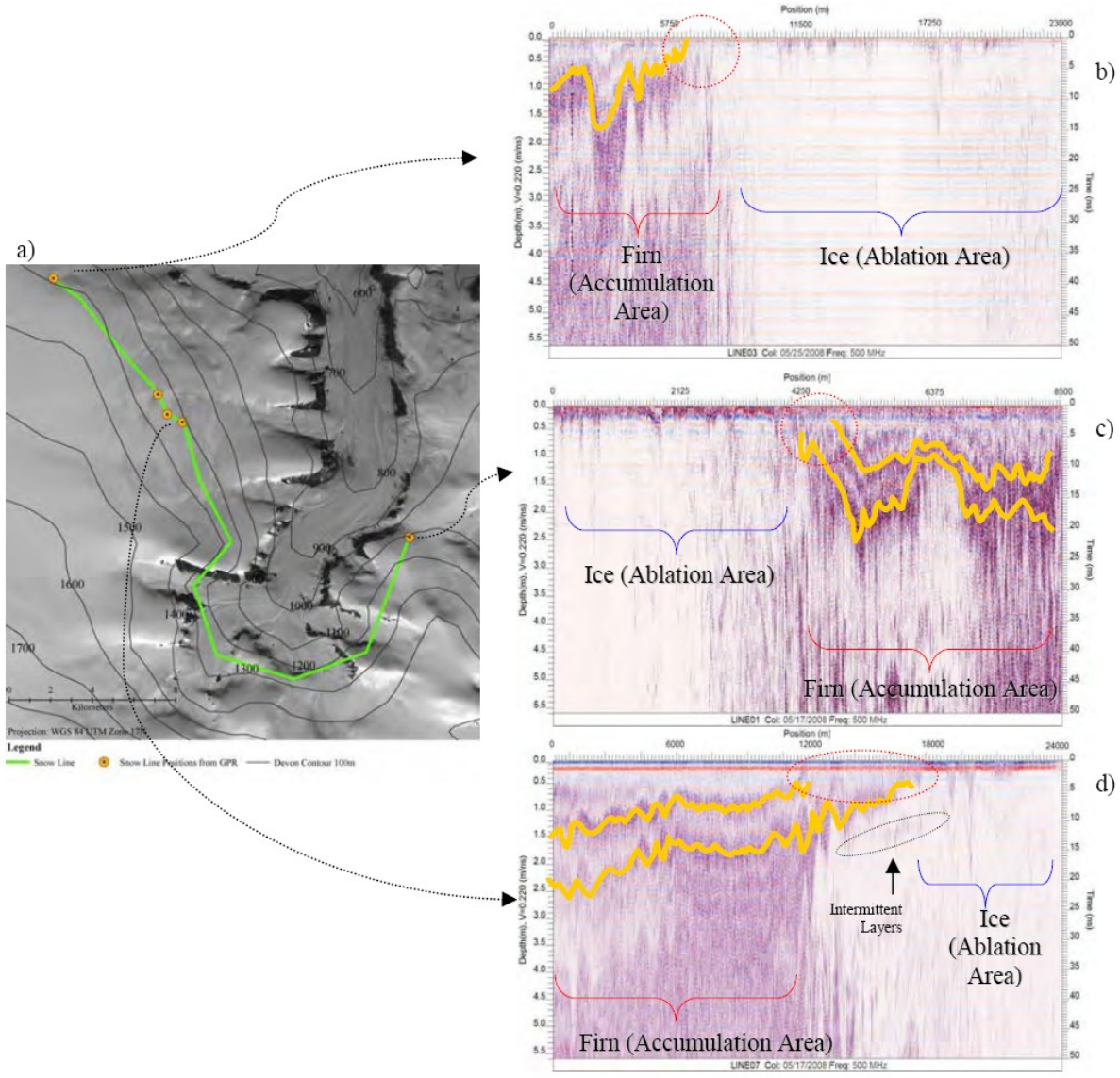

Figure A1. Image from Sylvestre (2009) showing a) locations where the firn line was identified in spring 2008 with the 500MHz GPR in the Northeast sector of DIC (orange dots in the inset map). The green line connects firn line positions based on the 1250 to 1300 m contour indicating the approximate position of firn line across the Northeast sector. b) 500 MHz GPR ~23 km long by 5.5 m deep; firn line found at 1275 m c) 500 MHz GPR line ~8.5 km long by 5.5 m deep; firn line found at 1264 m, and d) 500 MHz GPR line ~ 24 km long by 5.5 m deep; firn line found at 1271 m.

a)

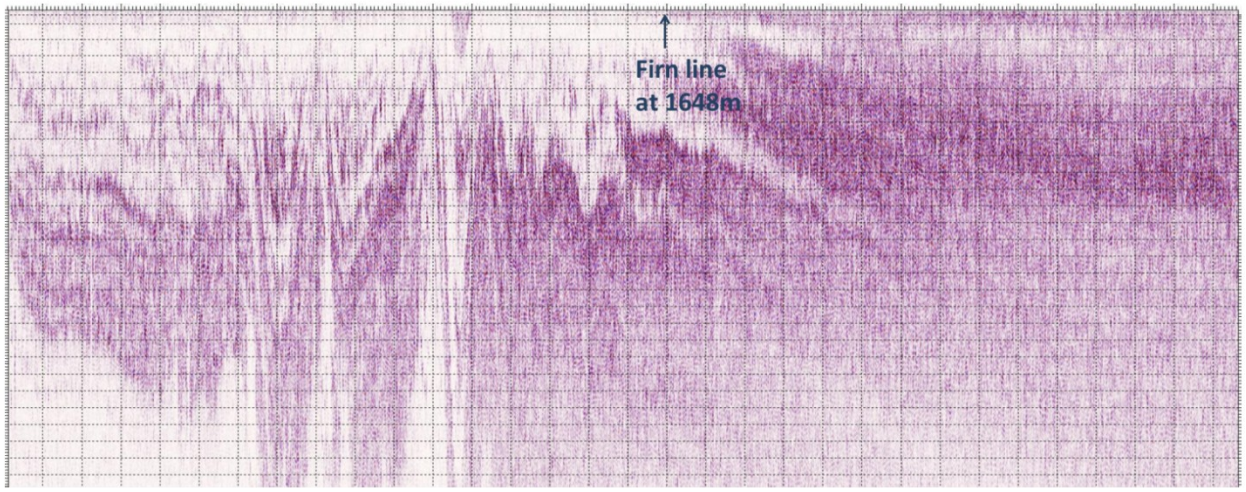

b)

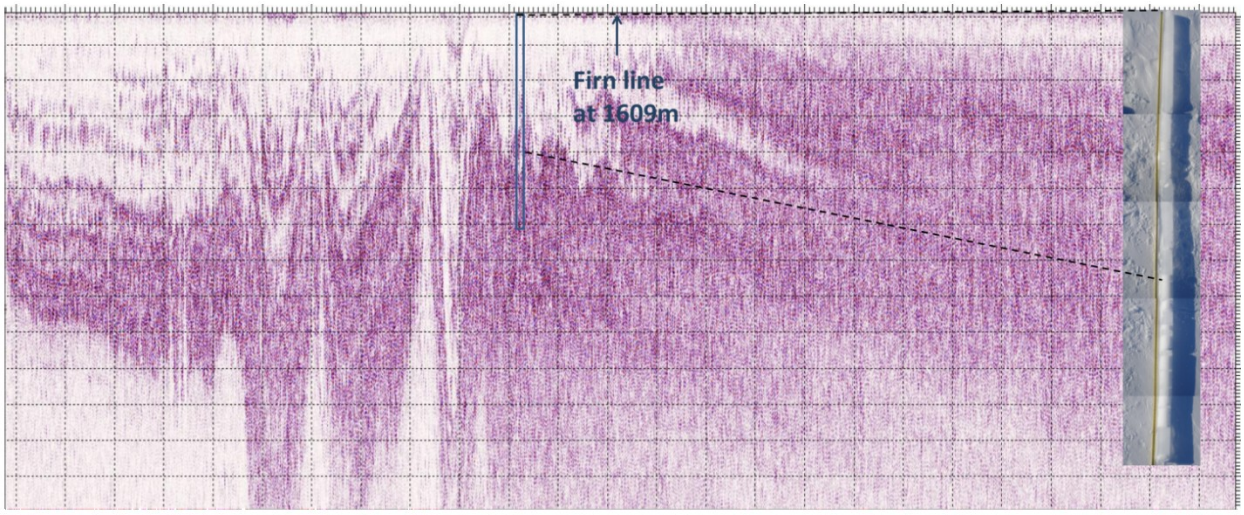

Figure A2. a) Radargram from the May 2012 GPR transect in the Northwest sector of DIC. b) Radargram from the May 2011 GPR transect in the Northwest Sector of DIC.